A Numerical Study of Stratospheric Gravity Waves Triggered by Squall Lines Observed during the TOGA COARE and COPT-81 Experiments

C. PIANI

Atmospheric, Oceanic, and Planetary Physics, Clarendon Laboratory, University of Oxford, Oxford, United Kingdom

D. R. DURRAN

Department of Atmospheric Sciences, University of Washington, Seattle, Washington

(Manuscript received 10 October 2000, in final form 22 June 2001)

ABSTRACT

A 3D mesoscale model is used to study the structure and intensity of stratospheric gravity waves generated by tropical convection. Two prototypical cases are examined: a squall line observed during the Tropical Ocean Global Atmosphere Coupled Ocean–Atmosphere Response Experiment (TOGA COARE) over the Pacific warm pool and a West African squall line observed during the Convection Profonde Tropicale 1981 (COPT-81) experiment. Gravity waves generated by these two squall lines are compared with those generated by a previously investigated event over northern Australia.

Although the individual squall lines vary in intensity, the stratospheric gravity waves generated by the various storms have surprisingly similar amplitudes. The similarity in the wave amplitudes arises because within each storm there is a positive correlation between the updraft intensity and the height of the level of neutral buoyancy. When the level of neutral buoyancy is relatively high, the atmospheric density in the region of wave generation is relatively low, and this reduction in density tends to weaken the convectively triggered waves thereby compensating for the stronger updraft velocities in the more intense storms.

The sensitivity of the azimuthal distribution of the convectively generated gravity waves to the upper-tropospheric and lower-stratospheric wind profile is also examined. In the absence of critical-level absorption, the motion of the storm relative to the stratospheric winds appears to be the single most important factor determining the azimuthal distribution of the waves. Stationary storm-relative waves, similar to mountain waves, may also be generated when there is a strong storm-relative stratospheric wind.

The interaction of the gravity waves with shear layers representative of the eastward and westward phases of the quasi-biennial oscillation (QBO) is also examined. An analysis of the domain-averaged momentum budget supports the claim that the drag exerted by critical-level absorption of convectively generated gravity waves plays a nontrivial role in the downward propagation of the QBO.

1. Introduction

Waves generated in the troposphere play an important role in the dynamics of the tropical stratosphere. In particular, the quasi-biennial oscillation (QBO) is driven by the deposition of Eliassen–Palm fluxes due to absorption of waves generated primarily at lower levels in the atmosphere. Recent studies have established that the downward propagation of the QBO cannot be driven by large-scale atmospheric waves alone, but is likely to depend on additional momentum transports by intermediate- and small-scale gravity waves (Dunkerton 1997; Baldwin et al. 2001). In the Tropics, the most likely source of intermediate- and small-scale gravity waves is deep convection.

Corresponding author address: C. Piani, Atmospheric, Oceanic, and Planetary Physics, Clarendon Laboratory, University of Oxford, Parks Road, Oxford OX1 3PU, United Kingdom.
E-mail: cpiani@atm.ox.ac.uk

Several studies based on rawinsonde observations have shown a positive correlation between seasonal variations in the intensity of tropical convection and the level of intermediate-scale gravity wave activity in the lower stratosphere (e.g., Vincent and Alexander 2000, which also contains a brief review of many additional studies). A direct link between convection and small-scale gravity-wave generation has been suggested by aircraft data collected along traverses above deep tropical convective systems (Alexander and Pfister 1995; Alexander et al. 2000); however, these data are not sufficiently dense in time and space to allow a complete characterization of the waves generated by the entire convective system.

Numerical simulations provide alternative means of examining the characteristics of convectively generated gravity waves and their probable influence on the QBO. Alexander and Holton (1997) conducted 2D simulations of a squall line observed during the Convection Pro-

© 2001 American Meteorological Society

fonde Tropicale (COPT-81) campaign and examined the propagation and dissipation of the gravity waves in the lower stratosphere triggered by this storm. They found that critical-level absorption of the gravity waves in the QBO shear layers produced a maximum decelerative forcing of roughly 5 m s^{-1} day^{-1} on the mean flow averaged over a 900-km-wide domain. As noted by Alexander and Holton (1997), considerable uncertainties are encountered when using the results from 2D simulations to estimate the true impact of convectively generated gravity waves on the QBO. Nevertheless, Alexander and Holton (1997), were able to arrive at a rough estimate that convectively triggered gravity waves could account for up to 25% of the forcing required to drive the QBO.

Recent papers by Piani et al. (2000, hereafter PDAH) and Lane et al. (2001) extended the study of stratospheric gravity-wave forcing by deep tropical convection to three dimensions. Both of these studies simulated the generation of waves during strong convective events, known as ''Hectors,'' which occur off the northwestern coast of Australia. Lane et al. (2001) focused on the dynamical processes responsible for gravity-wave generation by individual convective cells within the overall mesoscale convective system (MCS). PDAH, on the other hand, concentrated on the structure and characteristics of the convectively generated waves as they propagated through the lower stratosphere and encountered shear layers typical of the eastward and westward phases of the QBO. PDAH found that critical-level absorption of these gravity waves in the eastward-phase QBO shear layer induced a maximum decelerative forcing of 1 m s^{-1} day^{-1} on the mean flow averaged over a 500 km $\times$ 500 km domain. The maximum decelerative forcing in the westward-phase QBO shear layer was 0.3 m s^{-1} day^{-1}. Although these values are considerably less than those obtained in the 2D simulations of Alexander and Holton (1997), PDAH's estimate of the overall impact of convectively generated gravity-wave drag on the QBO, obtained from a more detailed climatology of tropical convection than that considered in Alexander and Holton (1997), remains consistent with the idea that convectively triggered gravity waves could account for roughly 25% of the forcing required to drive the QBO.

In this study we use the same 3D mesoscale model used by PDAH to examine the structure of the gravity waves triggered by additional examples of deep tropical convection: a squall line observed during the Tropical Ocean and Global Atmosphere Coupled Ocean–Atmosphere Response Experiment (TOGA COARE) over the Pacific warm pool and a second squall line that occurred during the COPT-81 experiment over the northern Ivory Coast (the same case considered in 2D by Alexander and Holton 1997). We also refine the description of the stratospheric wind profiles representing the eastward and westward phases of the QBO using a climatology of monthly mean stratospheric wind observations, and we repeat the Hector simulations of PDAH for these more representative wind profiles. The same set of stratospheric wind profiles (constant, eastward-phase QBO and westward-phase QBO) is thereby used to compare the propagation and dissipation of waves generated by three examples of tropical convection (TOGA COARE, COPT-81, and Hector).

A brief overview of the numerical model and spectral analysis procedure follows in section 2. Basic results from the TOGA COARE and COPT-81 simulations are presented in sections 3 and 4, respectively. The momentum transports and stratospheric momentum budgets for all three types of storms are compared in section 5. Section 6 is devoted to the analysis of stationary gravity waves generated by the convection in the TOGA COARE storm. The probable influence of convectively generated gravity-wave drag on the QBO is discussed in section 7. Section 8 provides a summary and the conclusions.

2. Research tools and methodology

a. Numerical model

In this study we use the same 3D mesoscale model adopted by PDAH. The equations of the model are presented and described therein. As in PDAH, simulations with both periodic and open lateral boundary conditions were performed. The open lateral boundary conditions are similar to those discussed by Fovell et al. (1992). A radiation condition is imposed at the upper boundary (Durran 1999, 427–431). The horizontal size of the computational domain is 540 $\times$ 660 km for the TOGA COARE experiment and 540 $\times$ 540 km for the COPT-81 experiment. In both cases the domain size extends from the ground to $z = 42$ km. Different horizontal domain sizes are due to the different size of the storms and to the limits on our computational resources. To keep each storm centered in the computational domain, the numerical domain translates at a constant horizontal velocity equal to the average speed of propagation of the deep convective cells. The translation speeds were $(u, v) = (10.4, -7)$ and $(-8, -2)$ in the TOGA COARE and COPT-81 cases, respectively.

The horizontal grid size is uniform with $\Delta x = \Delta y =$ 2000 m, while the vertical grid is stretched from $\Delta z =$ 100 m at the surface to $\Delta z = 400$ m at $z = 6$ km and above. The integration time step is $\Delta t = 4$ s for the TOGA COARE experiment and $\Delta t = 5$ s for the COPT-81 experiment. The chosen time steps are simply the largest ones that will not lead to numerical instabilities. The procedure used to initiate the convection will be discussed in connection with each individual storm.

b. Spectral analysis

Three-dimensional spectral analysis was performed on the wave-induced perturbations in the stratosphere.

Due to limitations on computational resources, the model-output data were subsampled in space and time. Values of a given variable α were archived every 3 min, from $t_0 = 15\,000$ s to $t_1 = 25\,000$ s, onto a grid with $\Delta x = \Delta y = 4$ km and $\Delta z = 1.2$ km. The resulting dataset constitutes a 4D array in longitude, latitude, height, and time $\alpha(x_i, y_j, z_k, t_n)$. This dataset was used to obtain a vertically averaged 3D power spectrum in zonal wavenumber, meridional wavenumber, and frequency $\langle\hat{\alpha}(\kappa_i, l_j, \omega_n)\rangle$.

The procedure for calculating the 3D spectra is the natural extension of the one used to calculate the 2D spectra presented in PDAH. Accordingly, we take the discrete Fourier transform of the variable $\alpha(x, y, z, t)$ with respect to x, y, and t to obtain $\tilde{\alpha}(\kappa, l, z, \omega)$. Letting * denote the complex conjugate, the height-dependent power spectrum of α is calculated as

$$\hat{\alpha}(\kappa, l, z, \omega) = \tilde{\alpha}(\kappa, l, z, \omega)\tilde{\alpha}^*(\kappa, l, z, \omega),$$

and the cospectrum of two variables, α and β, is

$$\widehat{\alpha\beta}(\kappa, l, z, \omega) = \mathrm{Re}\{\tilde{\alpha}(\kappa, l, z, \omega)\tilde{\beta}^*(\kappa, l, z, \omega)\}.$$

The resulting spectra include a redundancy in that $\hat{\alpha}(\kappa, l, z, \omega) = \hat{\alpha}^*(-\kappa, -l, z, -\omega)$. Consistent with the usual convention for eliminating redundancy in multidimensional propagating waves, we retain only the $\omega < 0$ part of the spectrum and associate the negative sign on ω with the negative sign in the time-dependence of the exponential in a wave of the form $e^{i(\kappa x + ly - \omega t)}$. According to this convention, waves with eastward and northward phase propagation will have wavenumbers $\kappa > 0$, $l > 0$.

Let angle brackets denote a density-weighted vertical average. The z-dependence in the spectral density is removed by averaging over the layer beginning at the top of the region of stratospheric wind shear ($z = 26$ km) and terminating at ($z = 40$ km) such that $\langle\hat{\alpha}\rangle$ is computed as

$$\langle\hat{\alpha}(\kappa, l, \omega)\rangle = \frac{1}{(k_2 - k_1)\rho(z_1)} \sum_{k=k_1}^{k_2} \rho(z_k)\hat{\alpha}(\kappa, l, z_k, \omega). \quad (1)$$

This spectrum is normalized to satisfy the discrete Parseval relation:

$$\sum_{i=-I/2}^{I/2} \sum_{j=-J/2}^{J/2} \sum_{n=0}^{N/2} \langle\hat{\alpha}(\kappa_i, l_j, \omega_n)\rangle = \sum_{i=1}^{I} \sum_{j=1}^{J} \sum_{n=1}^{N} \langle\alpha^2(x_i, y_j, t_n)\rangle. \quad (2)$$

Here, $x_1 = 0$, $x_I = L_x$, $y_1 = 0$, $y_J = L_y$; $\kappa_{I/2}$, $l_{J/2}$ and $\omega_{N/2}$ are the highest resolved zonal wavenumber, meridional wavenumber and frequencies respectively, and (t_1, t_N) is the time interval used for spectral analysis.

We should point out that this simple application of Fourier analysis has its limitations. Perhaps, the most important is that, if the wave field is composed of several distinct wave packets, the horizontal scale of the distinct packets may appear in the spectra as a low wavenumber bias.

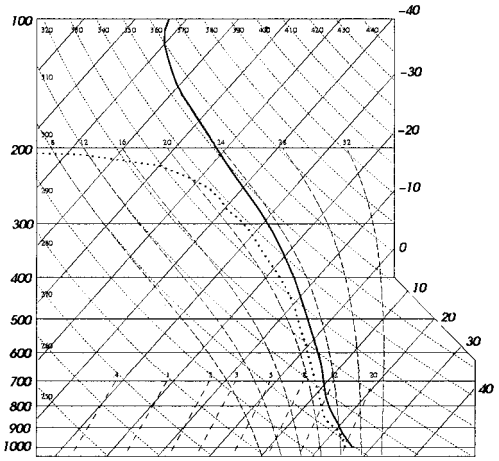

FIG. 1. Sounding from Trier et al. (1996), representative of the prestorm environment of a convective event triggered on 22 Feb 1993 over the southern area of the TOGA COARE site.

3. The TOGA COARE squall line

The TOGA COARE field observing program took place in the tropical western Pacific Ocean during November 1992–February 1993. The squall line studied in this work was observed over the southeastern portion of the TOGA COARE area near the Solomon Islands on 22 February 1993. During the 3-h period over which intensive observations were collected, the squall line was initially aligned roughly perpendicular to the low-level vertical wind shear and then evolved into a 3D bow shape. The line subsequently weakened and dissipated while moving eastward towards Guadalcanal (Trier et al. 1996).

a. Initialization

The thermodynamic sounding used in these simulations is representative of the prestorm environment of the observed squall line. This sounding, which is shown in Fig. 1 (also see appendix A for a tabulated version), was obtained from a blend of the 1800 and 2400 UTC 22 February Hoinara soundings and the aircraft data. A detailed description of the data used to produce this sounding is given by Trier et al. (1996). The convective available potential energy (CAPE) in the sounding is 1500 J kg^{-1}, and the tropopause is at approximately 15 km. The tropospheric wind profile (Fig. 2) was obtained from the same data used for the thermodynamic sounding. Low-level vertical shear is provided by a eastward 12 m s^{-1} jet. Above 2 km, the shear reverses and the winds ultimately become westward at the tropopause [u(tropopause) $= -5$ m s^{-1}]. The meridional wind component is zero above $z = 17$ km.

The zonal wind profiles used to represent eastward

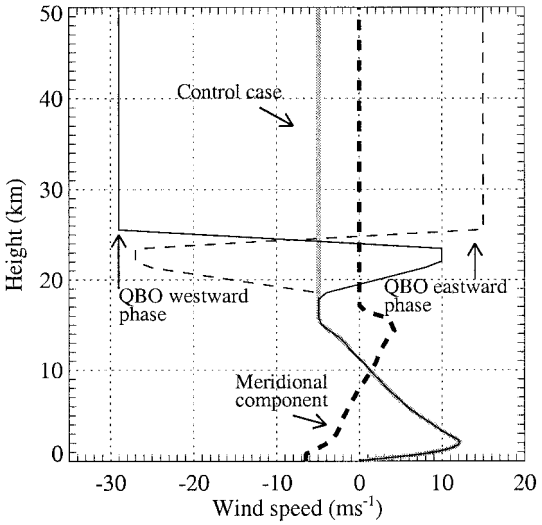

FIG. 2. Background wind profiles used in the TOGA COARE simulations. The thick, solid gray line is the zonal wind profile used in the control case. The thin solid lines are the zonal wind profiles used in the eastward phase QBO (dashed line) and westward phase QBO (solid line) cases. The thick dashed line is the meridional wind profile for all three cases.

and westward phases of the QBO were obtained from a dataset of monthly mean equatorial stratospheric zonal wind profiles taken at Canton Island (2°46′S 171°43′W, for the period Jan 1953–Aug 1967), Gan–Maledive Islands (0°41′S 73°9′E, Sep 1967–Dec 1975), and Singapore (1°22′N 103°55′E, Jan 1976–Apr 1999).[1] All the profiles from this dataset with strong eastward shear between $z = 20$ km and 30 km are overlaid in Fig. 3a. These profiles were not simply averaged to create the eastward-phase QBO profile because the different vertical positions of the shear layers in the individual soundings produce an overly smooth average that is not representative of the typical shear. Instead the profiles are fitted with a curve constrained to have no more than two shear layers of 3-km depth each. Two shear layers are allowed because almost all profiles with a prominent shear layer also feature an underlying layer that is a weaker remnant from the previous phase in the opposite direction. A representative profile for the westward phase of the QBO is obtained in a similar fashion (Fig. 3b). These profiles of the stratospheric wind speed are more representative of actual QBO profiles than those used previously in PDAH.

The initialization procedures of the TOGA COARE simulation are similar to those detailed in Trier et al. (1996). Convection is triggered by the collapse of a central cold anomaly consisting of a line of six partially overlapping smoothed cylinders with a temperature perturbation of -8°C aligned along the 330°–150° axis. Each cylinder is 1.4 km high and has a 10-km radius. They overlap in such a way that the border of each cylinder passes through the centers of the adjacent ones. The initial updrafts, triggered by the collapse of the cold cylinders, dissipate after about 3000 s and are replaced by a series of vigorous updrafts along the eastern and southern edges of the expanding cold pool. After roughly 10 000 s, the updrafts have gone through several cycles and their number and location is completely uncorrelated with the detailed structure of the initial cylinders.

Different initialization procedures were tested, including cold pools and warm bubbles of different strength and vertical extent. Not all initialization pro-

[1] Courtesy of Barbara Naujokat, Institut fuer Meteorologie, Freie Universitaet Berlin, Carl-Heinrich-Becker-Weg 6-10, D-12165, Berlin (E-mail: naujokat@strat01.met.fu-berlin.de).

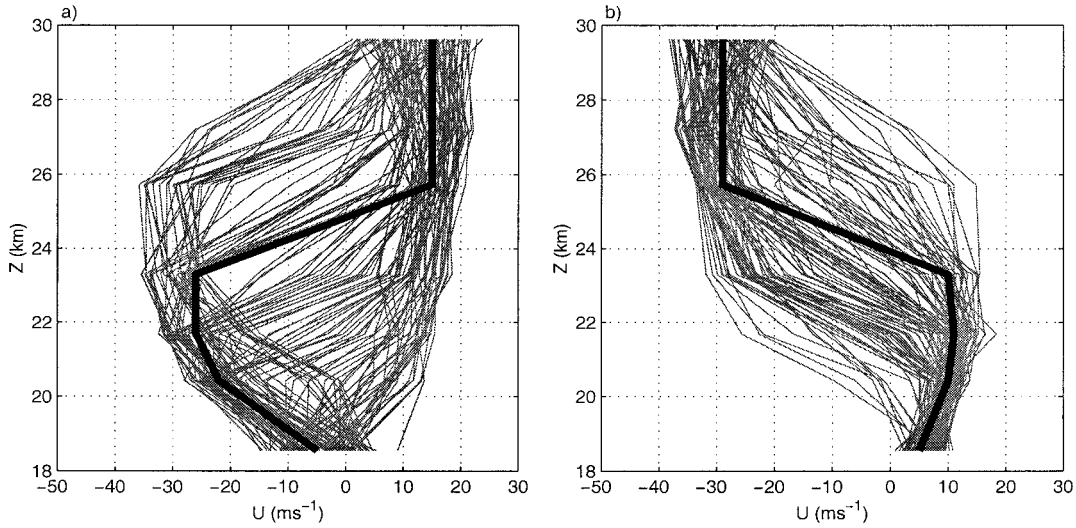

FIG. 3. Selected profiles of monthly mean zonal winds in the tropical stratosphere from the Naujokat Dataset (thin lines; see footnote 1) and profiles chosen for the simulations (thick lines): (a) eastward QBO phase, and (b) westward QBO phase.

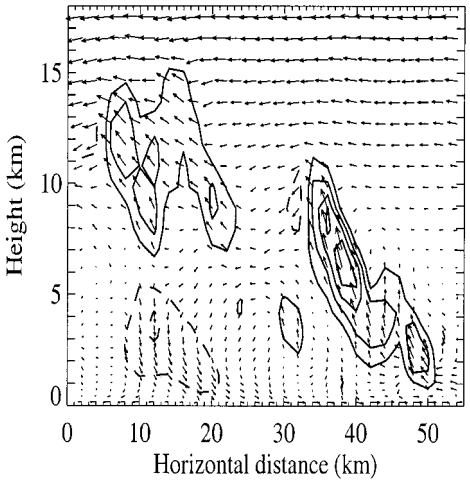

FIG. 4. Vertical velocity (1 m s^{-1} contour intervals; positive values solid, negative values dashed) and approximate storm relative flow obtained as the meridional average, with 300 km $< y <$ 340 km, roughly perpendicular to the central portion of the gust front at $t =$ 15 000 s. The gust front is positioned near the 50-km tickmark on this cross section.

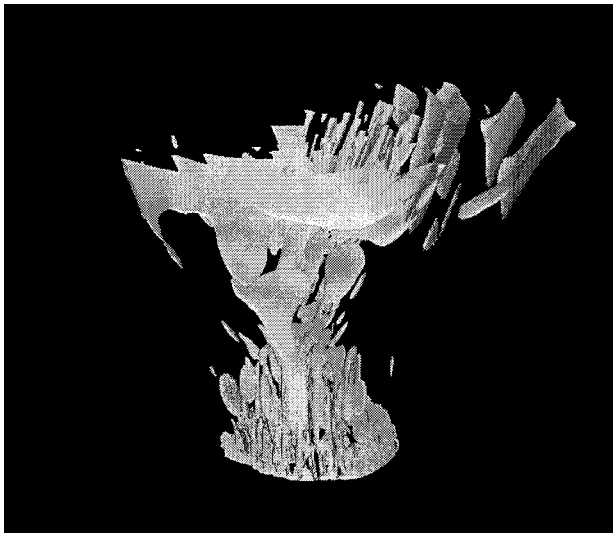

FIG. 5. Isosurfaces of vertical velocity ($w = 0.2$ m s^{-1}) obtained from the TOGA COARE control case at $t =$ 15 000 s. The storm is viewed from the *southeast,* which is the side with the strongest convection. The domain shown extends from the ground to 42 km.

cedures produce a long-lived organized squall line; however, when long-lived organized convection is produced, the storms and the stratospheric waves they generate become very similar within 2–3 h after initialization. The initial perturbation described above was chosen because it produced organized quasi-steady convection quickly and because it was the same one used by Trier et al. (1996).

b. Simulation overview

The most vigorous convection takes place along the southern portion of the gust front, which is aligned perpendicular to the low-level shear. The maximum updrafts along this region of the gust front are on the order of 10 m s^{-1} and never exceed 15 m s^{-1}. These vertical velocities are similar to the peak updrafts observed during the actual storm, which ranged between 10 m s^{-1} and 15 m s^{-1} (Trier et al. 1996). Some idea of the updraft structure within the storm is provided in Fig. 4, which shows contours of the vertical velocity and storm-relative wind vectors in an east–west cross section perpendicular to the central portion of the gust front. The data plotted in Fig. 4 represent a 40-km average in the north–south direction through the center of the domain (nominally an average parallel to the gust front), and as such, they may be directly compared with the data in Fig. 14 of Trier et al. (1996), which shows both Doppler radar observations and the Trier et al. simulation for the same storm. Both the updraft and the general flow structure are qualitatively similar between the observations and the two numerical simulations. No observations pertaining to the storm-generated stratospheric gravity waves were collected. A more detailed comparison of the three-dimensional non steady structures within the simulated and observed convective systems is beyond the scope of this paper and will not be presented here. Nevertheless, this brief comparison of observed and calculated updraft speeds and structures should be adequate to establish that the our simulated storm is at least representative of those occurring in the TOGA COARE region.

Isosurfaces of vertical velocity from the control case (i.e., the case with no stratospheric wind shear) at $t =$ 15 000 s are shown in Fig. 5. The southern portion of the gust front appears as a continuous wall at the base of the storm. A region of vigorous updrafts appears just behind the gust front. Gravity-wave induced velocity perturbations appear above the region of deep tropospheric updrafts as truncated sections of concentric cones. The same basic features may be seen in the vertical and horizontal cross sections shown in Fig. 6.

It is apparent from these figures that nearly all of the wave activity is in eastward and southward propagating waves. This asymmetry appears to be due to the east-southeastward motion of the updrafts relative to the stratospheric flow. It is difficult to precisely determine a characteristic horizontal speed for the updrafts because different sections of the storm propagate in different directions with different speeds. In particular, the cells on the northern side of the system tend to propagate with a northward component relative to the center of the system, while the motion of those cells on the southern side exhibits a southward component. Even the horizontal motion of an individual updraft varies with time. Nevertheless, the storm as a whole propagates at an average ground relative speed of $u = 10.4$ m s^{-1} and $v = -7$ m s^{-1}. We stress that this is not the speed of the gust front that moves outward relative to this frame

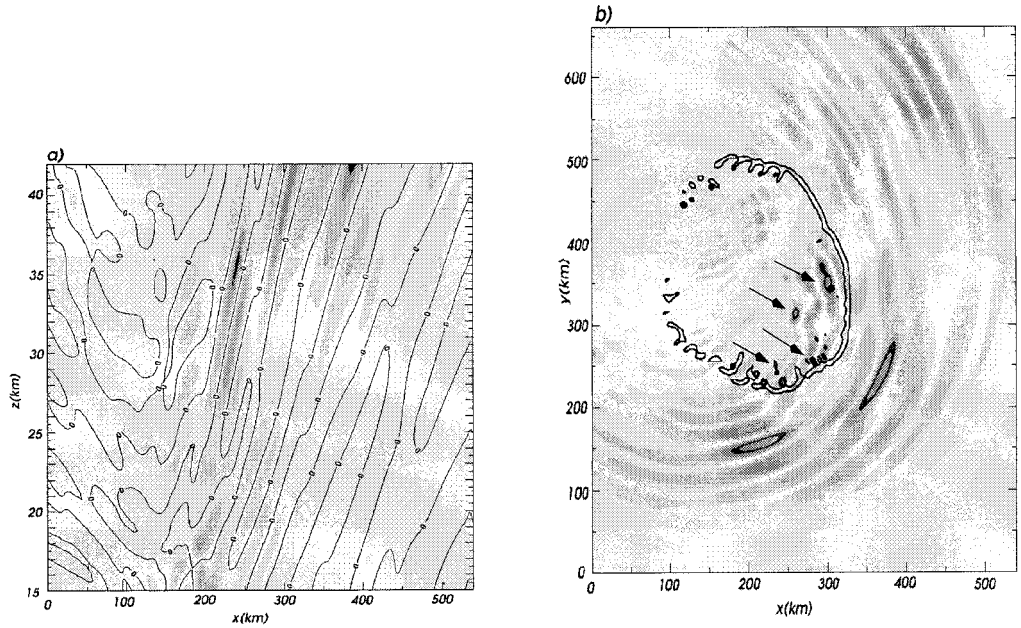

FIG. 6. (a) Vertical–zonal cross section through the lower stratosphere at $t = 15\,000$ s and $y = 350$ km. The shaded field is the *magnitude* of the vertical velocity. The shading interval is 0.1 m s^{-1} and the thin solid line is the 0 contour. (b) Horizontal cross section of the entire domain at $t = 15\,000$ s. The shaded field is the *magnitude* of the vertical velocity at $z = 40$ km. The thick line is the 0.2 m s^{-1} contour of vertical velocity at $z = 200$ m, which shows the location of the gust front. The thickest contours just behind the southern and eastern edges of the gust front (arrows) enclose compact regions of strong latent heating at $z = 8$ km.

of reference at a roughly 2–3 m s^{-1}.[2] Using these values, the storm-relative stratospheric winds for the TOGA COARE control case are $u = -15.4$ m s^{-1} and $v = 7$ m s^{-1}.

[2] The speed of the observed storm steadily increased from 11 to 14 m s^{-1} during its lifetime (Trier et al. 1996). These values bracket the 12.5 m s^{-1} translation speed of the storm in the numerical simulation.

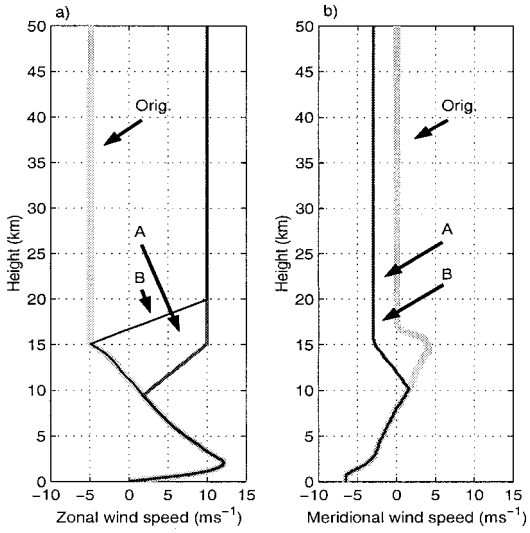

FIG. 7. Background zonal (a) and meridional (b) wind profiles used in the control case and two modified TOGA COARE simulations.

The dependence of the storm-generated wave field on the storm-relative stratospheric wind was examined by repeating the control simulation with several different mean wind profiles in which the storm-relative stratospheric winds were progressively reduced. The zonal and meridional wind profiles used in two of these simulations (cases a and b) are plotted in Fig. 7 together with the profile for the control case. In case a southeastward shear was added between 10 and 15 km, and the resulting storm-relative stratospheric wind components are roughly $u = 0$ m s^{-1} and $v = 3$ m s^{-1}. The storm-relative stratospheric winds in b are the same as in a; the only difference between a and b is in the winds between 10 and 20 km. In a the ground-relative winds never become eastward, whereas in both b and in the control case, the wind drops to -5 m s^{-1} at $z = 15$ km. The convectively generated gravity waves appear to emanate from a region near the level of neutral buoyancy, which for the TOGA COARE case is near $z = 12$ km, so the changes in the environmental wind profiles introduced in cases a and b are located almost entirely above the level of wave generation.

Horizontal cross sections of the magnitude of the vertical velocity at $z = 40$ km from simulations a and b are shown in Fig. 8. Comparison of this figure with Fig. 6b shows that the azimuthal distribution of wave activity at $z = 40$ km is much more isotropic in cases a and b than it is in the control case. Moreover, the similarity of the wave patterns in cases a and b suggests that critical level filtering in the layer of westward shear just

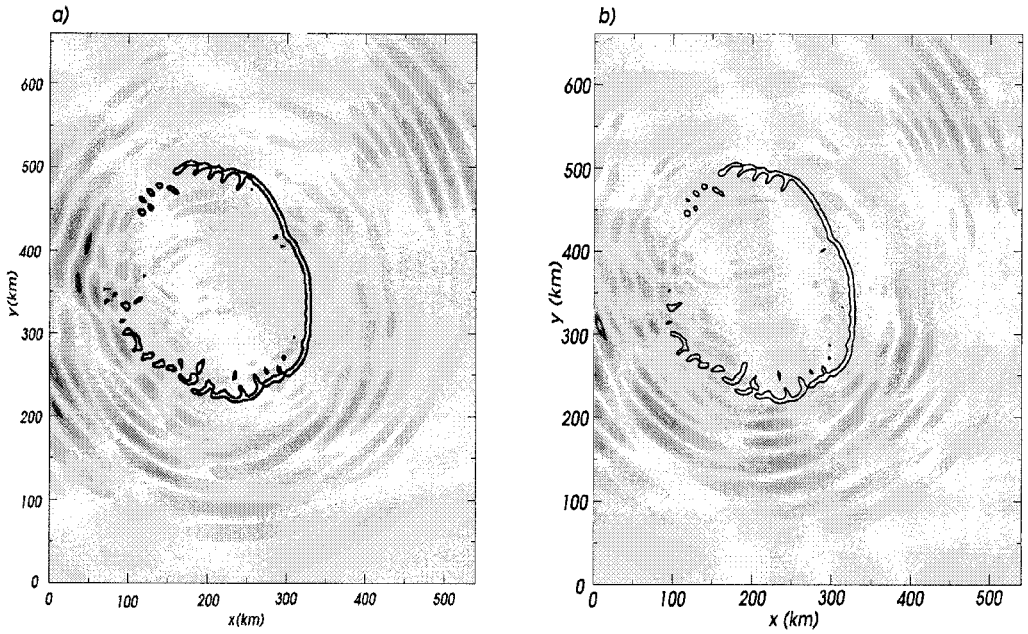

FIG. 8. As in Fig. 6b but with background wind profiles A and B shown in Fig. 7.

above the wave-generation region is not an important factor in reducing the amplitude of the westward propagating waves in the control case. More generally, the full series of simulations, from which a and b were selected for presentation, suggest that (at least for moderate variations in the wind profile) the azimuthal distribution of wave activity at some level elevated above the convection depends mostly on the horizontal motion of the convective updrafts relative to the flow at that elevated level and not on the details of the wind profile between the elevated level and the level of wave generation. This result, that in the absence of critical-level filtering the storm-relative stratospheric wind is the primary factor determining the horizontal distribution of convectively generated stratospheric gravity waves, is consistent with results obtained in two-dimensional simulations by Beres et al. (2002, manuscript submitted to *J. Atmos. Sci*).

Now we consider the influence of the idealized QBO shear layers on the propagation of convectively generated gravity waves. Figure 9 shows contours of the magnitude of the vertical velocity field, in the same vertical and horizontal cross sections plotted in Fig. 6, for the eastward-phase QBO TOGA COARE simulation. The eastward traveling waves in this simulation are refracted and partially damped as they cross the main stratospheric shear layer centered at roughly 25 km. A pronounced decrease in eastward wave activity, relative to that in the control simulation, is apparent in the eastward-phase QBO case at $z = 40$ km; (cf. Figs. 6b and 9b). In contrast, there is no obvious difference in westward-propagating wave activity between the control and the westward-phase QBO simulations (cf. Figs. 6b and 10b). No difference in the amplitude of the westward propagating waves is evident between the control case and the westward-phase QBO simulations because the relatively weak westward propagating waves that are present in these two simulations exit through the western boundary before arriving at $z = 40$ km. On the other hand, the intrinsic frequencies of the eastward propagating waves in the westward-phase QBO simulation do increase as they pass through the westward-shear layer and, consistent with the conservation of wave action, at $z = 40$ km these waves are stronger than those in the control case.

c. Spectral analysis

A more quantitative assessment of the azimuthal distribution of those convectively generated gravity waves that penetrate through the QBO shear layers can be obtained by examining the power spectrum of the vertical velocity $\langle \hat{w}(k, l, \omega) \rangle$, as defined by (1). For ease in visualization, the full three-dimensional spectrum is reduced to a function of the horizontal wavenumbers k and l by averaging over ω. Contours of the base-10 logarithm of the average of $\langle \hat{w} \rangle$ over ω for the TOGA COARE control case appear in Fig. 11. The same quantity is plotted for the eastward and the westward phases of the QBO in Figs. 12a,b. Plotting the logarithm rather, than the function itself, makes it easier to see the distribution of the weaker waves.

Consistent with the contours of w at $z = 40$ km shown in Figs. 6b, 9b, and 10b, westward traveling waves (i.e., waves with $k < 0$) are virtually absent in all the simulations. In the control case (Fig. 11), the wave energy

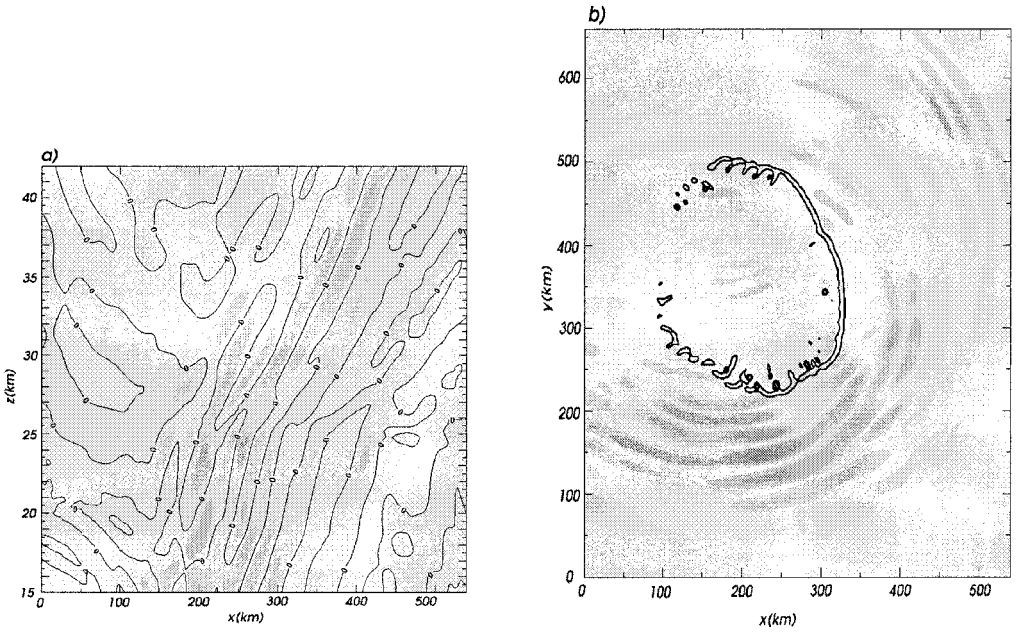

FIG. 9. Like Fig. 6 but for the eastward phase of the QBO.

is distributed approximately equally over all the waves with nonnegligible eastward phase propagation and is concentrated at horizontal wavenumbers between $0.01 < (\kappa^2 + l^2)^{1/2} < 0.02$ cycles km^{-1}, corresponding to horizontal wavelengths between 50 and 100 km.

The eastward shear in the eastward phase of the QBO produces a small but noticeable decrease in the amplitude of the eastward moving waves in Fig. 12a. Although the eastward propagating waves are still clearly dominant, a general decrease in spectral power is present over the entire $\kappa > 0$ portion of the spectrum. Recalling that $\log_{10}\langle\hat{w}\rangle$ is plotted in Fig. 12a, there appears to be almost an order of magnitude decrease in the spectral power of the most energetic waves between the control simulation and the eastward-phase QBO simulation.

Since no significant westward propagating waves are present, the only effect of the westward shear in the westward phase of the QBO is to amplify the eastward

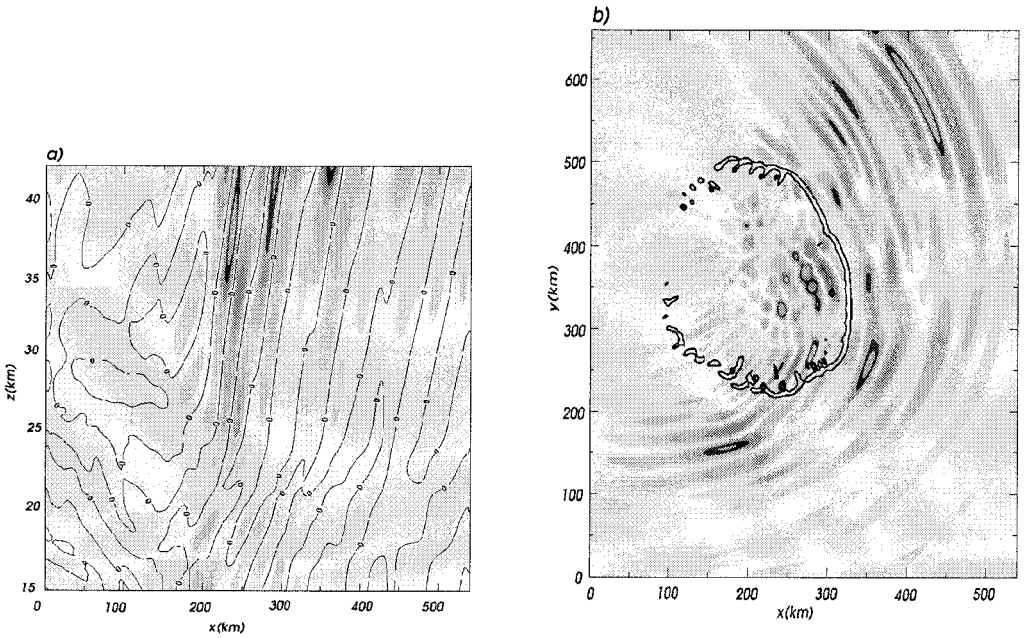

FIG. 10. Like Fig. 6 but for the westward phase of the QBO.

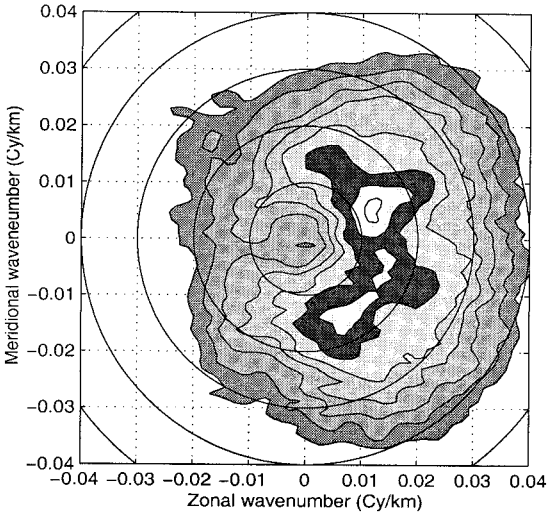

FIG. 11. Contours of $\log_{10}\langle\hat{w}\rangle$ averaged over ω as a function of the zonal and meridional wavenumbers (κ, l) for the TOGA COARE control simulation. The concentric circles are contours of total horizontal wavenumber $(\kappa^2 + l^2)^{1/2}$, hence the first inner circle represents wavelengths of 100 km, the second represents wavelengths of 50 km, etc. Darker shades generally correspond to lower values, with a contour interval of 0.5. However, the third highest level has been highlighted with a particularly dark shade to allow easy identification when comparing with the following two figures.

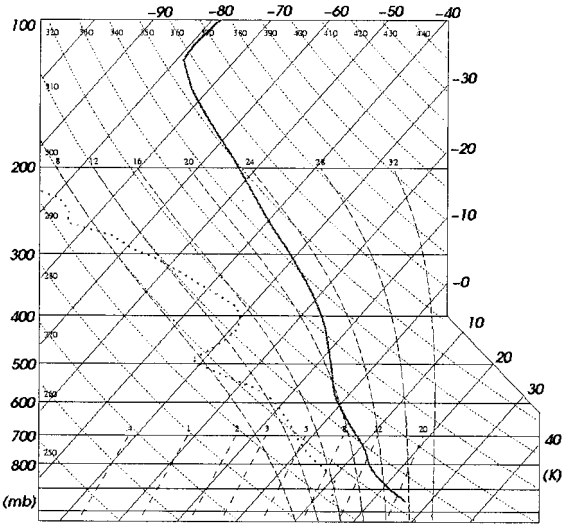

FIG. 13. Sounding obtained from Roux (1988), representative of the prestorm environment of a convective event triggered on 23 Jun 1981 over northern Ivory Coast during COPT-81.

propagating waves. This difference in amplitude, which is consistent with conservation of wave action, is apparent for the most energetic waves shown in Fig. 12b.

4. The COPT-81 squall line

On 23 June 1981 a particularly intense squall line reached the COPT-81 site on the northern Ivory Coast. The squall line was oriented along the northwest–southeast axis moving southwest at roughly 14 m s^{-1}. The strongest measured updrafts were between 15 and 20 m s^{-1}. The updrafts formed along the leading edge of the squall line and propagated northeast (rearward) at roughly 3 m s^{-1} relative to the gust front. After roughly 2∼3 h the storm moved away from the site towards the Atlantic Ocean (Roux 1987).

a. Initialization

The thermodynamic sounding used to specify the initial conditions in these simulations is representative of the environment over northern Ivory Coast at 2332 UTC[3] 23 June 1981 (Fig. 13). The CAPE is quite high,

[3] UTC coincides with local time on the Ivory Coast.

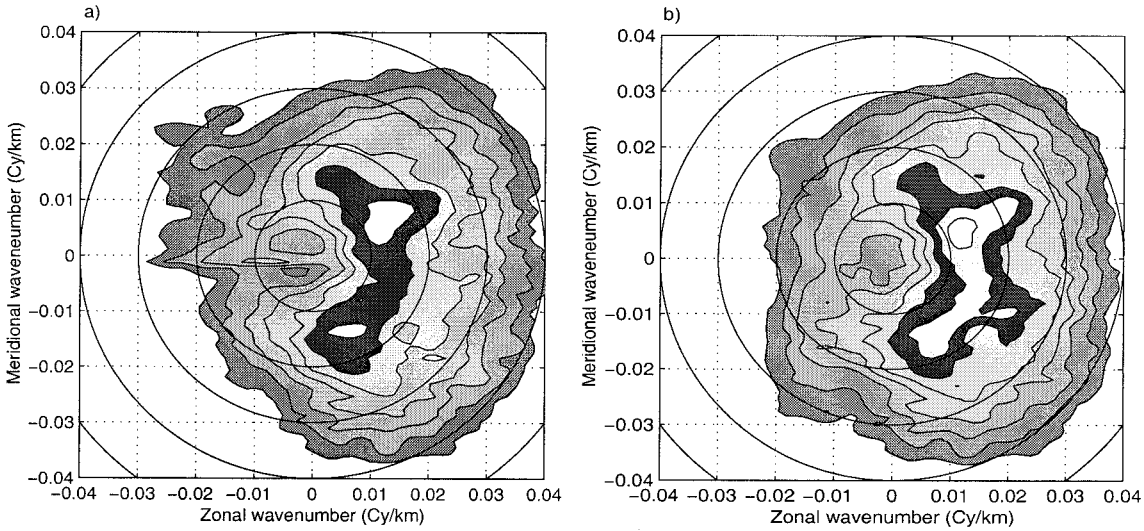

FIG. 12. As in Fig. 11 but for (a) the eastward-phase QBO simulation and (b) the westward-phase QBO simulation.

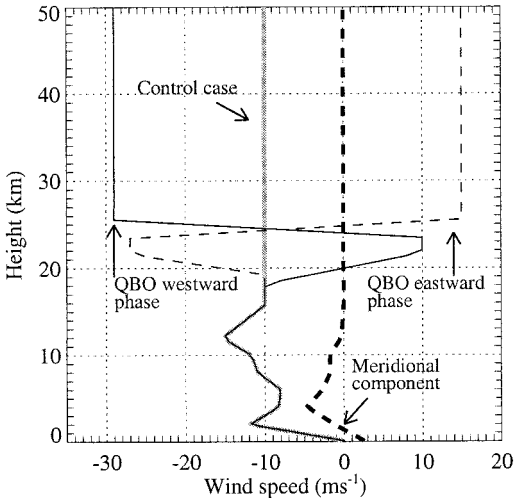

FIG. 14. Background wind profiles used in the COPT-81 simulations. The thick solid gray line is the zonal wind profile used in the control case. The thin solid lines are the zonal wind profiles used in the eastward phase QBO (dashed line) and westward phase QBO (solid line) cases. The thick dashed line is the meridional wind profile for all three cases.

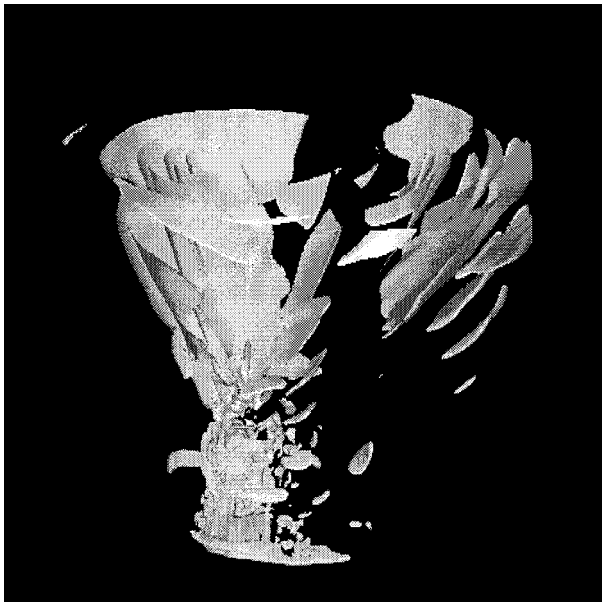

FIG. 15. Isosurfaces of vertical velocity ($w = 0.2$ m s^{-1}) obtained from the storm simulation 15 000 s after initialization. The storm is viewed from the *south.* The isosurface spans from the ground to 42 km in height, and approximately 540 km in diameter at the top.

at roughly 2810 J kg^{-1}, due mainly to the low-level moisture flowing in from the Atlantic. The tropopause is located at roughly 16-km height. The relatively dry layer at 500 mb favors the formation of intense downdrafts.

The initial tropospheric zonal wind profile used in this study is obtained as an average between the pre- and poststorm wind profiles used by Redelsperger and Lafore (1988) in their 3D model (Fig. 14). The zonal wind component is westward throughout the domain with a low level jet of -12 m s^{-1} (African Easterly Jet) and an upper tropospheric jet of -15 m s^{-1} (Tropical Easterly Jet). At the tropopause, the zonal wind component is -10 m s^{-1}. Above this point the winds are determined by one of the three stratospheric wind profiles. In the control case the zonal wind is constant at -10 m s^{-1} throughout the stratosphere. In the other two cases the zonal winds are the same ones used in the TOGA COARE experiments to represent the westward and eastward phases of the QBO. The meridional wind component is weak and southward in the troposphere and is zero above 12 km in all simulations.

Convection is initialized using a central surface cold pool comprised of four partially overlapping cylinders identical to the ones used to initialize the TOGA COARE simulations. The cylinders are aligned perpendicular to the direction of motion of the storm along the 166°–345° axis. Updrafts form at the intersections of the initial cylinders on both sides of the cold pool as the cylinders collapse. After roughly 3000 s the initial updrafts start to dissipate and new updrafts form only on the southwest side of the cold pool, which no longer bears resemblance to four distinct cylinders. As the second set of updrafts matures, a continuous gust front begins to develop at the leading edge. The most intense convection occurs just behind the gust front with updrafts on the order of 20 m s^{-1}, occasionally reaching reaching 25 m s^{-1}. After 10 000 s ($\sim$3 h) the updrafts have gone through several cycles and the storm seems to have reached a quasi steady state. The simulated storm propagates at a ground-relative speed of approximately 8 m s^{-1} to the west and 2 m s^{-1} to the south.

b. Simulation overview

Isosurfaces of the vertical velocity, obtained from the control case at $t = 15\,000$ s, are shown in Fig. 15. This figure is analogous to Fig. 5 for the TOGA COARE experiment. In this figure, the storm is viewed from the south. As in Fig. 5, the gust front is visible as a solid wall at the base of the storm. The southern portion of the gust front extends well to the east before dissipating. The strongest convection appears as elongated cells just behind the gust front. Above this region, gravity-wave-induced vertical velocity perturbations form nearly concentric cones. The distribution of these surfaces indicates that there is significant wave activity in both westward and eastward propagating waves.

Vertical and horizontal cross sections of the storm are shown in Figs. 16a,b. Westward traveling waves present a smaller angle to the vertical compared to their eastward traveling counterpart. This indicates a higher intrinsic frequency and a smaller vertical wave number (longer vertical wavelength). Since, westward and eastward traveling waves have different angles to the vertical and since we can make no assumptions on the

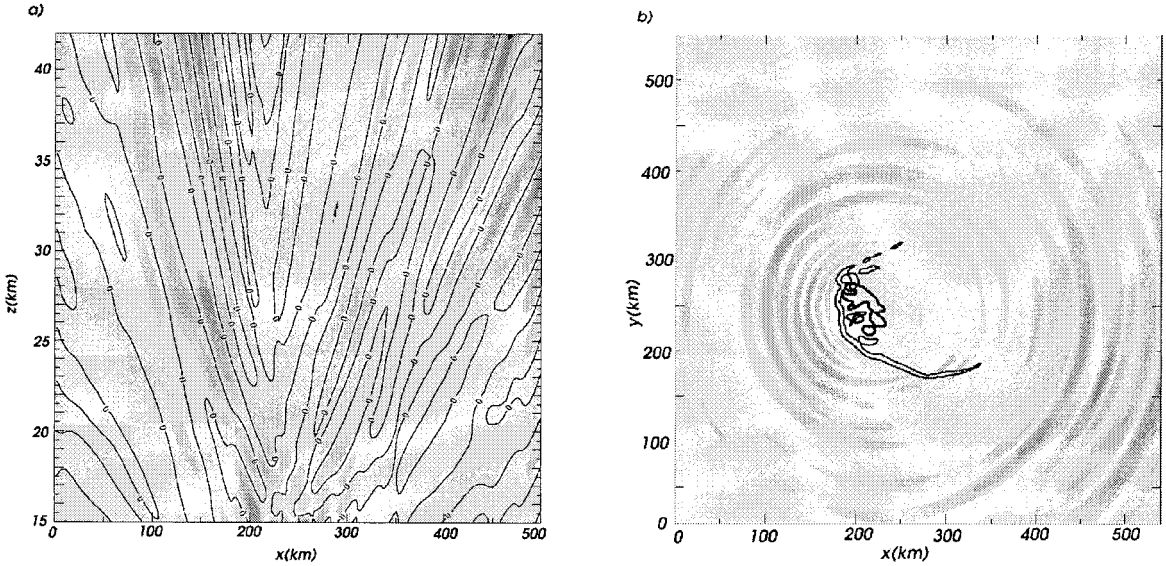

FIG. 16. (a) Vertical–zonal cross section at $t = 15\,000$ s and $y = 270$ km. The shaded field is the *magnitude* of the vertical velocity and the solid line is the 0 contour. The shading interval is 0.1 m s^{-1}. (b) Horizontal cross section of the domain at $t = 15\,000$ s and $z = 40$ km. The shaded field is the *magnitude* of the vertical velocity. The thick line is the 0.2 m s^{-1} contour of vertical velocity at $z = 200$ m. The thickest contours in the center of the figure enclose regions of strong latent heating at $z = 8$ km.

isotropy of the wave field at lower levels, close to the generation regions, the fact that the amplitude in the vertical velocity fluctuations associated with the waves traveling in one direction is larger does not imply that these waves are more energetic. All else being equal, waves propagating with a greater angle to the vertical will have smaller vertical velocity components. To further examine the directional dependence of wave activity, isosurfaces of zonal velocity are shown (Fig. 17).

FIG. 17. Like Fig. 15 but for the perturbation zonal velocity showing the isosurface $(u - \overline{u}) = 0.5$ m s^{-1}.

Vertical and horizontal cross sections of the magnitude of the zonal velocity are shown in Figs. 18a,b. These figures indicate that eastward traveling waves are characterized by larger fluctuations of zonal velocity.

In the eastward-phase QBO case the eastward propagating waves appear to be damped at roughly 25-km height (Fig. 19a). It is also apparent from the horizontal cross section (Fig. 19b) that virtually no eastward propagating waves reach the 40-km level. In the westward-phase QBO case the westward propagating waves also appear to be damped below 25-km height (Fig. 20a). This vertical cross section, however, passes through the center of the domain and misses some weak westward propagating waves that lie farther to the south. The shaded regions that appear west of the gust front on the horizontal cross section (Fig. 20b) indicate that westward propagating waves, with vertical velocities of at least 0.1 m s^{-1}, are still present at 40-km height.

c. Spectral analysis

As for the TOGA COARE cases, contours of the base-10 logarithm of the average of $\langle \hat{w} \rangle$ over ω for the COPT-81 control case are shown in Fig. 21 and for the eastward and westward phases of the QBO in Figs. 22a,b. By comparison with the TOGA COARE 2D spectra (Fig. 11), spectral energy in the COPT-81 control case (Fig. 21) shows a larger degree of horizontal isotropy. Most of the wave energy is concentrated at horizontal wavenumbers between $0.01 < (\kappa^2 + l^2)^{1/2} < 0.02$ cycles km^{-1}, corresponding to horizontal wavelengths between 50 and 100 km. A group of shorter and slower moving waves are visible on the top left portion of Fig. 21 with

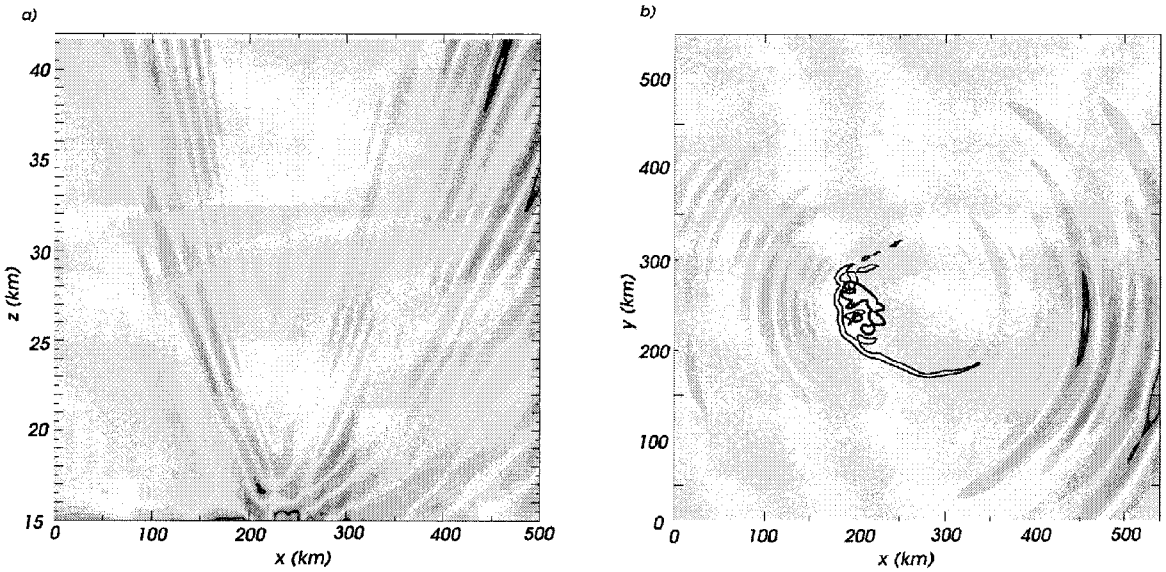

FIG. 18. (a) Vertical–zonal cross section at $t = 15\,000$ s and $y = 270$ km. The shaded field is the zonal wind speed. The shading interval is 0.5 m s^{-1}. (b) Horizontal cross section of the domain at $t = 15\,000$ s and $z = 40$ km. The shaded field is the zonal wind speed. The thick line is the 0.2 m s^{-1} contour of vertical velocity at $z = 200$ m. The thickest contours in the center of the figure enclose regions of strong latent heating at $z = 8$ km.

$0.02 < (\kappa^2 + l^2)^{1/2} < 0.03$ cycles km^{-1}, which corresponds to a horizontal wavelength between 30 and 50 km. These short waves are also visible in Fig. 16b just west of the gust front. Finally, there is comparatively little energy associated with waves traveling to the northeast of the storm.

The effects of stratospheric shear on the spectra are stronger though qualitatively similar to those in the TOGA COARE cases (cf. Figs. 22a,b and Fig. 21 with Figs. 12a,b and Fig. 11). In the case of eastward stratospheric shear (Fig. 22a) the eastward propagating waves ($\kappa > 0$) are damped while the westward propagating waves ($\kappa < 0$) are amplified. In the westward shear case (Fig. 22b) the westward propagating waves are damped, though not entirely, while the eastward propagating waves are amplified.

5. Momentum balancing

The momentum budget associated with gravity-wave propagation and dissipation in the stratosphere is in-

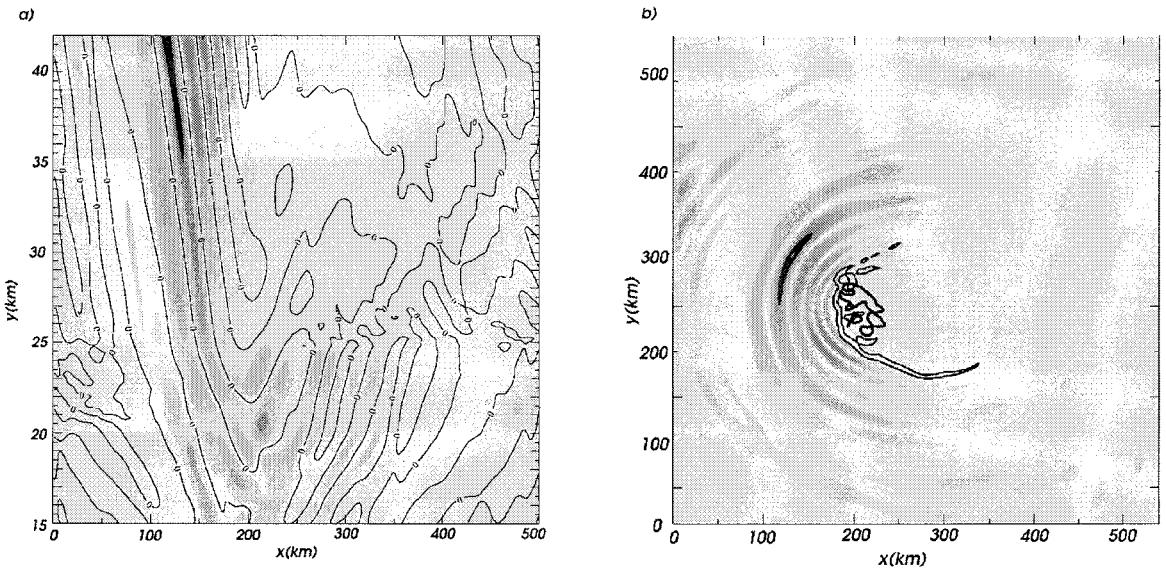

FIG. 19. Like Fig. 16 but for the eastward phase of the QBO.

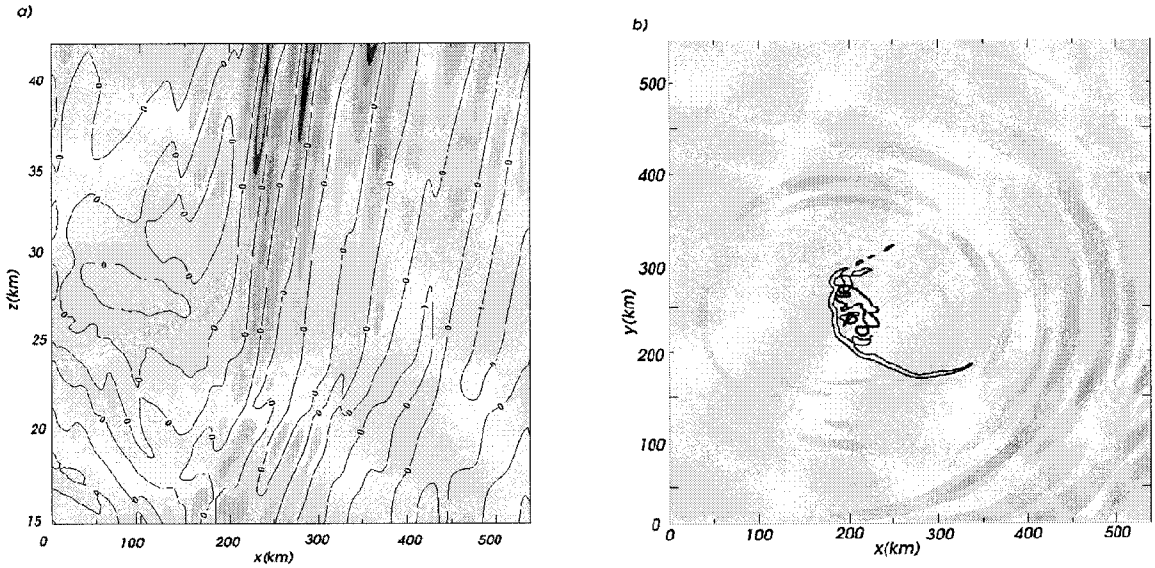

FIG. 20. Like Fig. 16 but for the westward phase of the QBO.

vestigated by examining individual terms in the zonal momentum equation:

$$\frac{\partial \rho u}{\partial t} + \frac{\partial \rho u^2}{\partial x} + \frac{\partial \rho u v}{\partial y} + \frac{\partial \rho u w}{\partial z} = -f\rho v - \frac{\partial p}{\partial x} + \rho M, \quad (3)$$

where u, v, and w are the total zonal, meridional, and vertical velocities, respectively; ρ is total density; p is total pressure; and M is the forcing due to subgrid scale mixing and smoothing. If we separate the dynamic variables into their horizontal mean and perturbation components ($u = \overline{u} + u'$; $v = \overline{v} + v'$; $w = \overline{w} + w'$; $p = \overline{p} + p'$), substitute into (3), and take the horizontal average for the case of a nonrotating atmosphere ($f = 0$), we obtain

$$\frac{\partial}{\partial t}\overline{\rho u} + \frac{1}{L_x L_y}\int_0^{L_y} (\rho u' u + p')_0^{L_x}\, dy + \frac{1}{L_x L_y}\int_0^{L_x} (\rho u' v)_0^{L_y}\, dx + \overline{w\rho}\frac{\partial \overline{u}}{\partial z} + \overline{u\left(\frac{\partial \rho u}{\partial x} + \frac{\partial \rho v}{\partial y} + \frac{\partial \rho w}{\partial z}\right)} + \frac{\partial}{\partial z}\overline{\rho u' w'} = 0, \quad (4)$$

where the overbars represent horizontally averaged quantities, $[\alpha]_\beta^\gamma$ is $\alpha(\gamma) - \alpha(\beta)$, and L_x and L_y are the east–west and north–south extent of the domain, respectively. The horizontal average of the mixing and smoothing term $\overline{\rho M}$ is zero since subgrid-scale mixing does not occur in the stratosphere and only horizontal smoothing is done on u.

The first term on the lhs is the horizontally averaged zonal momentum acceleration. The second term is the meridional average of the differential advection of zonal momentum plus the pressure difference between the east and west boundaries, this term will be referred to as a horizontal average of the ''dynamic-pressure gradient.'' The third term is the zonal average of the differential meridional advection of zonal momentum between the north and south boundaries. The fourth term is the vertical advection of momentum by the mean vertical velocity. The fifth term on the lhs is proportional to the horizontally averaged density fluctuations ($\overline{u}\partial\rho/\partial t$). Finally, the last term on the lhs is the horizontally averaged

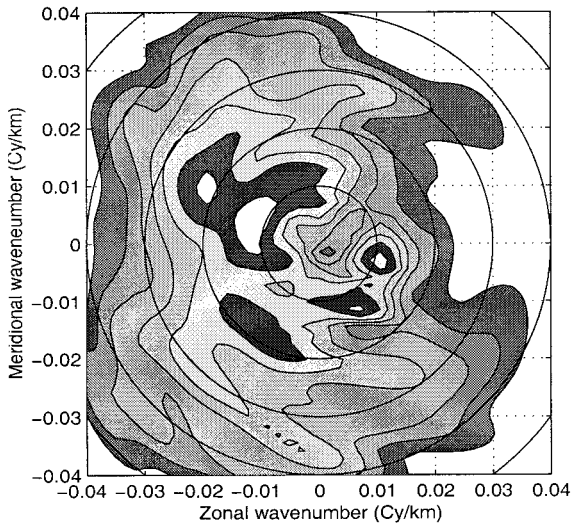

FIG. 21. Contours of $\log_{10}\langle \hat{w} \rangle$ averaged over ω as a function of the zonal and meridional wavenumbers (κ, l) for the COPT-81 control simulation. The concentric circles are contours of total horizontal wavenumber $(\kappa^2 + l^2)^{1/2}$, hence the first inner circle represents wavelengths of 100 km the second represents wavelengths of 50 km, etc. Darker shades generally correspond to lower values, with a contour interval of 0.5. However, the second highest level has been highlighted with a particularly dark shade to allow easy identification when comparing with the following two figures.

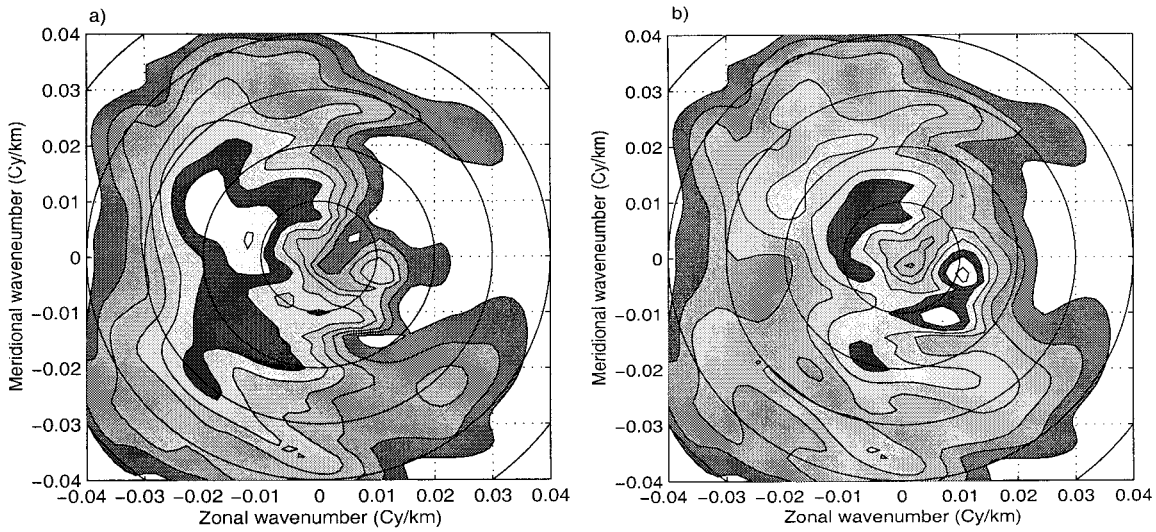

FIG. 22. (a) Like Fig. 21 but for the eastward-QBO phase case and (b) the westward-QBO phase case.

divergence of the vertical flux of zonal momentum. After evaluation, the third and fifth terms on the lhs of (4) turned out to be an order of magnitude smaller than the rest.

PDAH observed that the response to momentum-flux convergence due to gravity-wave dissipation in a series of open-boundary simulations was dominated by a large dynamic-pressure difference across the domain that approximately balanced the mean-flow acceleration (see Figs. 14a,b of PDAH); the vertical momentum-flux convergence, itself, constituted a smaller term in the volume-averaged momentum budget. In this study we obtained similar results in our open-boundary simulations (not shown). Nevertheless, the atmosphere is horizontally periodic and the vertical divergence of the zonal momentum fluxes observed in these simulations would, therefore, be expected to produce a change in the zonal momentum averaged around an entire latitude circle. As in PDAH, we will therefore examine the volume-averaged momentum budget in simulations performed in horizontally periodic domains.

Vertical profiles of the largest terms of the horizontally averaged zonal momentum equation (4) are shown in Fig. 23. The profiles in Fig. 23 represent time averages over the period between 15 000 and 25 000 s, during which the waves generated by the convection exhibited a quasi-steady distribution. Figures 23a,d show the results from the eastward- and westward-QBO phase TOGA COARE cases, respectively. Similarly, Figs. 23b,e show the results from the eastward- and westward-QBO phase simulations of the COPT-81 storm. To facilitate comparison with the results from PDAH, we repeated their periodic-boundary simulations with the same QBO shear profiles used in this study; the results for the eastward and westward phases of the QBO with this modified profile (hereafter referred to as the Hector case) are shown in Figs. 23c,f. Small terms, whose profiles would appear as indistinguishable clutter around the $x = 0$ axis, have been omitted from all the plots shown in Fig. 23. In each panel, the thick solid line is the acceleration of the mean zonal wind and the thick dashed line is the vertical momentum-flux divergence. The thin solid line, offset to the right, is the mean-zonal wind profile. Though the later is not plotted with any reference scale it serves the purpose of identifying the levels of shear.

The most obvious characteristic of these profiles is that the vertical momentum-flux divergence [last term on the lhs of Eq. (4)] is almost exactly balanced by the mean zonal wind acceleration [first term on the lhs of Eq. (4)]. When comparing the various simulations, one must keep in mind that values shown in Fig. 23 represent horizontal averages over domains of slightly different size and that the total momentum deposited by wave dissipation is diluted in proportion to the horizontal extent of their domains. The domain sizes for the Hector, TOGA COARE, and COPT-81 simulations are 500×500, 540×660, and 540×540 km, respectfully. Hence, the TOGA COARE and COPT-81 domains are roughly 1.42 and 1.17 times larger than the Hector domain.

In all six panels there appears to be significant momentum-flux divergence at the principal shear levels (at $z \approx 25$ km) and, to a lesser extent, at the weaker secondary shear levels (at $z \approx 20$ km). In all the shear regions the sign of the zonal mean wind acceleration is such that the shear layer would propagate downward. However, no significant downward propagation of the shear layers is observed during the course of these simulations, which is not surprising since the timescale of the QBO is roughly 2000 times longer than the duration of these simulations. The strongest accelerations are in the principal shear layers of the COPT-81 and Hector cases with peaks at roughly 2 m s^{-1} day^{-1} in the eastward phase of the QBO (Figs. 23b,c) and roughly -1

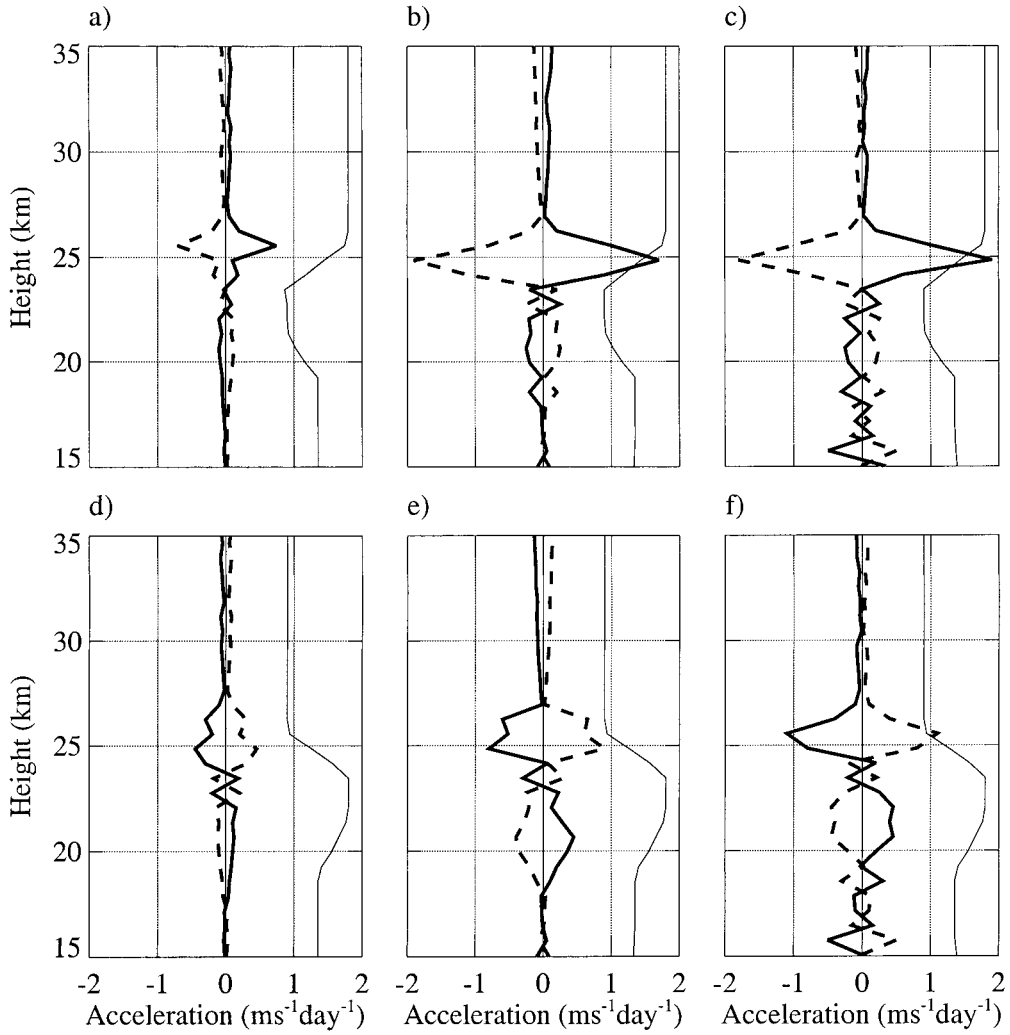

FIG. 23. Vertical profiles of the largest terms of the time and horizontally averaged zonal momentum equation. The thick solid line is the acceleration of the mean zonal wind while the thick dashed line represents the vertical momentum-flux divergence. The thin solid line, offset to the right and out of scale, is the mean zonal wind profile. Eastward-QBO phase simulations for (a) TOGA COARE, (b) COPT-81, and (c) Hector. Westward-QBO phase simulations for (d) TOGA COARE, (e) COPT-81, and (f) Hector.

m s^{-1} day^{-1} in the westward phase of the QBO (Figs. 23e,f). The accelerations in the TOGA COARE experiment are weaker by comparison, even when the domain size is taken into account, with peaks at roughly ± 0.5 m s^{-1} day^{-1} in both the eastward and westward phases of the QBO (Figs. 23a,d).

The basic character of the flow acceleration shown in each panel of Fig. 23 can be anticipated by examining the magnitude of the horizontal momentum flux carried by the waves as a function of the storm-relative phase speed of those waves. The storm structure and, therefore, the distribution of the convectively triggered gravity waves entering the lower stratosphere are almost independent of the stratospheric wind profile. Thus, the the most accurate diagnosis of the momentum flux carried by the waves triggered in a given series of simulations (i.e., the Hector, TOGA COARE, or COPT-81 series) is obtained from the control case in which there is no stratospheric wind shear and it is easy to compute a meaningful vertically averaged cospectrum of $\langle u'w' \rangle$ (with the averaging computed over the range 26 km $< z <$ 40 km). The distribution of horizontal momentum flux as a function of storm-relative phase speed in each control case was determined as follows. First, the (κ, $l = 0$, ω) plane of the 3D cospectrum of u' and w' was interpolated onto a finer mesh of (κ, ω) points. Then the values of ω/κ were binned into intervals of width dc_x, where $c_x = \omega/k$ is the storm-relative phase speed (or trace speed) along to the x axis. Next, a set of ordered pairs $[c_x, m(c_x)]$ was created by defining $m(c_x)$ as the sum of all spectral values $\widehat{\langle u'w' \rangle}$ (κ, ω) for which $c_x - dc_x/2 < \omega/\kappa > c_x + dc_x/2$. Finally, the magnitude of

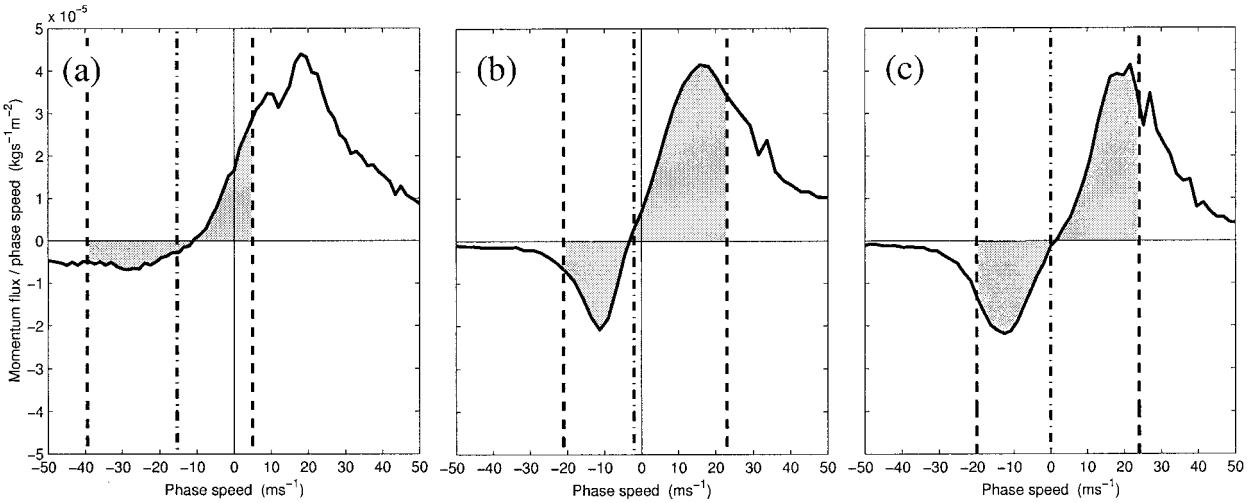

FIG. 24. Zonal momentum flux density $m(c_x)$ as a function of storm-relative zonal phase speed for the control case with periodic lateral boundaries for (a) TOGA COARE, (b) COPT-81, and (c) Hector. The thick dashed lines are the storm-relative winds above the shear layers in the eastward- and westward-phase QBO cases. The thick dot–dashed line is the storm-relative stratospheric wind in the control case. Shaded areas represent the momentum flux lost by the waves while crossing eastward- and westward-phase QBO shear layers.

$m(c_x)$ was normalized such that its global integral with respect to c_x is equal to the average vertical momentum flux over the total horizontal domain, over the vertical layer between $z = 26$ and 40 km, and over the period between 15 000 and 25 000 s; that is;

$$\int_{-100}^{100} m(c_x)\, dc_x = \frac{1}{10\,000} \int_{15\,000}^{25\,000} \overline{\langle \rho u' w' \rangle}\, dt. \quad (5)$$

The upper and lower limits of ± 100 m s^{-1} on c_x are sufficiently large that the integral captures almost all the wave-induced momentum flux. By construction, $m(c_x)$ is a momentum flux density function, hence $m(c_x)dc_x$ is the momentum flux associated with waves of phase speed between $c_x - dc_x/2$ and $c_x + dc_x/2$.

Figure 24 shows plots of the zonal momentum-flux density as a function of the (storm-relative) horizontal gravity-wave phase speed for the COPT-81, TOGA COARE, and Hector control simulations. Also indicated by thick dashed vertical lines are the maximum (u_{max}) and minimum (u_{min}) storm-relative stratospheric wind speeds in the eastward and westward phases of the QBO. The constant storm-relative stratospheric wind in the control case is shown by the thick dot–dashed line. To the extent that these time-averaged $x - z$ momentum fluxes represent the momentum transport by steady linear 2D gravity waves that vanish far upstream and downstream from the convection, the Eliassen–Palm theorem guarantees that the fluxes will be constant with height except at a critical level. Based on the standard theory of small-amplitude waves approaching a critical level, all eastward propagating waves with phase speeds in the interval (0, u_{max}) (positive shaded regions) should encounter critical levels and be almost entirely absorbed within the shear layer in the eastward-phase QBO simulations. Similarly, westward propagating waves with phase speeds in the interval (u_{min}, 0) (negative shaded regions) should experience critical-level absorption in the westward-phase QBO simulations. In addition, there is also some wave absorption at critical levels in the secondary shear layer of both phases of the QBO, so that a limited range of eastward propagating waves are absorbed in the westward phase of the QBO, and vice versa.

Figure 24b shows that, consistent with Fig. 16, considerably more momentum flux is carried by the eastward propagating waves than by the westward propagating waves in the COPT-81 simulations. Only a little more than half of the momentum flux transported by eastward moving waves is propagated at phase speeds less than u_{max}, whereas most of the momentum flux carried by westward moving waves satisfies $u_{min} < c_x$. Nevertheless, the momentum transported by eastward moving waves that encounter critical levels in the eastward-phase QBO simulation still exceeds the momentum transported by the westward moving waves encountering critical levels in the westward-phase QBO simulation. This asymmetry is roughly consistent with the difference between the mean-flow acceleration in the eastward- and westward-phase COPT-81 simulations evident in Figs. 23b,e. A similar asymmetry in the eastward and westward momentum flux and mean-flow acceleration is apparent for the Hector profiles in Figs. 24c and 23c,f.

The TOGA COARE case shown in Fig. 24a is somewhat different. The asymmetry between the momentum flux carried by the eastward and westward propagating waves is more pronounced than in the other two cases, although only a relatively small portion of the momen-

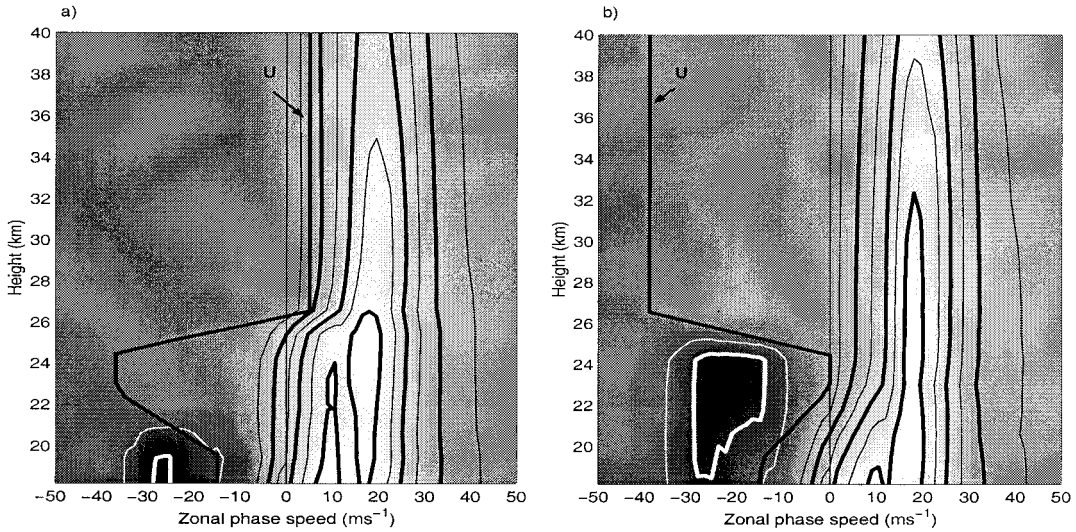

FIG. 25. Momentum-flux density as a function of height and storm-relative phase speed for the periodic boundary TOGA COARE simulations with (a) the eastward-phase QBO, or (b) the westward-phase QBO. Lighter shades of gray (contoured with black) represent positive (eastward) momentum flux while darker shades of gray (contoured in white) represent negative (westward) momentum flux. The thick solid lines shows the profile of the storm-relative mean zonal wind.

tum flux carried by eastward propagating waves is transported at phase speeds less than $u_{\max}$. Thus consistent with Figs. 23a and 23d, there is less mean-flow acceleration in either QBO phase of the TOGA COARE cases than in the COPT-81 and Hector cases.

After comparing the amplitude of the eastward and westward waves in Fig. 6 one might wonder why Fig. 24a shows any amplitude in the momentum flux carried by westward propagating waves. The difference in the strength of the westward propagating waves indicated in these two figures is due to a difference in the lateral boundary conditions. Figure 6 shows the wave distribution in an open boundary simulation, whereas Fig. 24a gives results computed in a periodic domain. The equivalent of Fig. 24a for the open-boundary simulation shows no power in the momentum flux carried by waves moving westward relative to the storm (not shown). Apparently a significant number of westward traveling waves exit the domain in the open-boundary TOGA COARE simulation. The difference in the wave distribution between the open- and periodic-boundary simulations is less pronounced in the COPT-81 and Hector cases.

The preceding arguments are based on the theoretical result that small-amplitude waves approaching a mean-state critical level at which Ri $\gg 1/4$ undergo absorption. To assess how well small-amplitude theory actually accounts for finite-amplitude wave-induced momentum deposition in the QBO shear layers in these simulations, the momentum-flux density (5) was recomputed without vertical averaging and contoured as a function of c_x and z in Fig. 25 for the TOGA COARE QBO-shear cases. The lighter shades of gray (contoured in black) in Fig. 25 represent positive (eastward) momentum flux while darker shades of gray (contoured in white) represent negative (westward) momentum flux. Superimposed on the shaded fields are the vertical profiles of the mean zonal wind (plotted using the same horizontal scale as c_x) for the eastward phase of the QBO (Fig. 25a) and the westward phase of the QBO (Fig. 25b). As evident from Fig. 25, the mean wind does form an effective barrier to vertical momentum transport by waves with phase speeds such that $|c_x| < |\overline{u}|$.

6. Stationary waves

Unlike the control simulations for the COPT-81 and Hector cases, in the TOGA COARE control simulation there is a significant storm-relative stratospheric flow and significant momentum flux, roughly 40% of the peak value, is carried by waves with zero storm-relative phase speed (see the value for $c_x = 0$ in Fig. 24a). Mason and Sykes (1982) and Clark et al. (1986) have suggested that, if an updraft has nonzero velocity relative to the local winds at the level of neutral buoyancy, gravity waves may be generated through an obstacle effect similar to that which produces mountain waves. The structure of the gravity waves with zero storm-relative phase speed in the TOGA COARE control simulation can be appreciated by comparing the vertical velocity at $z = 40$ km as revealed by a snapshot at $t = 15\,000$ s (Fig. 26a) with a time average of the same field over the interval $15\,000 \leq t \leq 25\,000$ s in the storm-relative frame of reference (Fig. 26b). The time resolution used to compute this average was 3 min. In contrast to the instantaneous distribution of the gravity waves, the largest amplitude waves in the time-averaged field are concentrated along a narrow band parallel to the mean

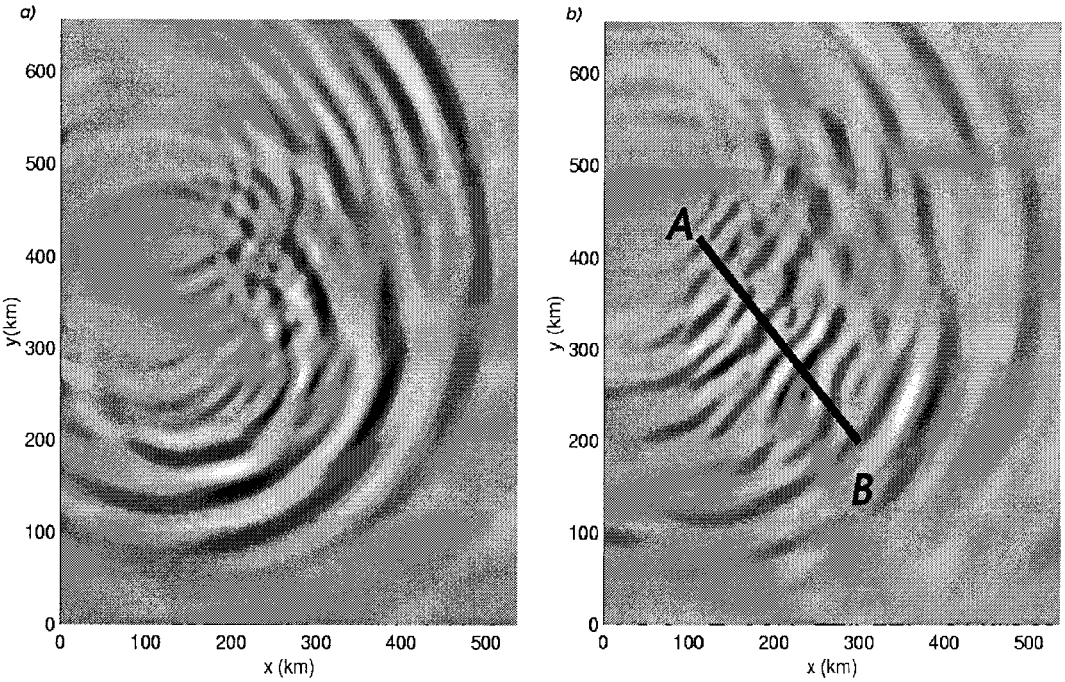

FIG. 26. (a) Snapshot at $t = 15\,000$ s of the vertical velocity at $z = 40$ km for the TOGA COARE control case. (b) Time average from $t = 15\,000$ s to $t = 25\,000$ s of vertical velocity at the same level (the shading scale has been magnified compared with Fig. 26a for clarity). The line segment AB indicates the location of the vertical cross section displayed in Fig. 27.

stratospheric wind, which blows parallel to the line AB in Fig. 26b. The wave crests and troughs within this band are oriented perpendicular to the mean wind.

Figure 27 shows the stratospheric velocity field in a vertical cross section parallel to the mean wind along part of line AB in Fig. 26b. As in Fig. 26b, these velocities are averaged between $t = 15\,000$ s and $t = 25\,000$ s in a frame of reference moving with the storm. The shaded field is vertical velocity; the vectors show the projection of the total velocity minus the mean stratospheric wind $(u + 15, v - 7, w)$ onto the plane of the cross section. As would be expected for upward propagating gravity waves generated by flow over a stationary obstacle, the phase lines tilt upstream. Consistent with the standard gravity-wave polarization relations (Gill 1982, p. 131), the perturbation velocity vectors in the plane of the vertical cross section are approximately parallel to the lines of constant phase. This indicates that the stationary storm-relative response does indeed have the structure of a vertically propagating gravity wave. Moreover the wave response is almost monochromatic with a horizontal wavelength on the order of 30–40 km, which is roughly the distance between the bursts of strongest updraft activity within the convective system (see Fig. 4). Interestingly, the dominant horizontal wavelengths in the instantaneous wave field (Figs. 6a and 26a) are approximate twice as long as those in which dominate the stationary storm-relative response.

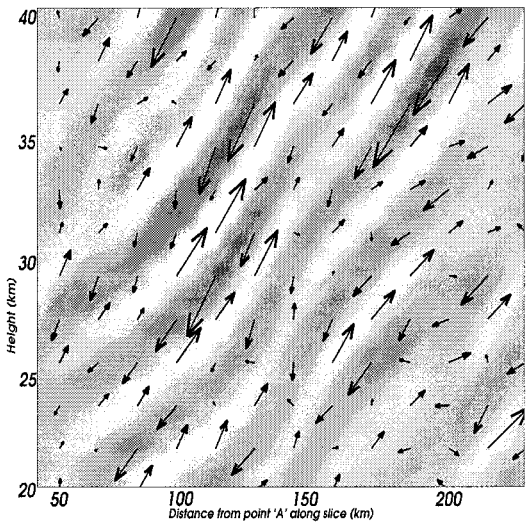

FIG. 27. Vertical cross section along segment AB shown in Fig. 26b. The time-averaged vertical velocity component is shaded; the vectors show the projection of the time-averaged perturbation velocity vector onto the plane of the cross section.

7. Discussion

The TOGA COARE, COPT-81, and Hector storms simulated in this work differ with respect to the strength

of their updrafts and their speed of propagation. The initial CAPE in the COPT-81 and Hector storms was roughly 2800 J kg^{-1}, while that in the TOGA COARE case was only 1500 J kg^{-1}. As a consequence, the maximum updrafts in the TOGA COARE simulation (15–20 m s^{-1}) were significantly weaker than those in the COPT-81 and Hector simulations (20–25 m^{-1}). Both the COPT-81 and Hector squall lines propagate westward at a speed similar to the environmental winds just above the tropopause. On the other hand, the TOGA COARE squall line propagates towards the southeast, and for this case, the storm-relative winds just above the tropopause are roughly -17 m s^{-1}.

Given the differences in CAPE and maximum updraft velocities, the amplitude of the stratospheric gravity waves triggered by each storm is surprisingly similar. In particular, at $z = 40$ km, the gravity waves triggered in the COPT-81 and Hector control cases and the eastward propagating gravity waves triggered by the TOGA COARE control case are of comparable magnitude (Figs. 5b and 15b; Fig. 4b in PDAH). Furthermore when the background wind profile in the TOGA COARE control simulation was modified so that the storm-relative stratospheric wind was nearly zero, both the eastward and westward propagating gravity waves had similar amplitudes to those in the Hector and COPT-81 experiments (Fig. 8).

The similarity in the amplitude of the waves aloft that were generated by the weaker TOGA COARE storm and the stronger COPT-81 and Hector events appears to be attributable to differences in the heights at which the waves are generated. Very close to the source, the amplitude of the vertical velocity perturbations in convectively triggered gravity waves are roughly proportional to the vertical velocities in the convective cells. As the waves propagate upward, away from the source, their amplitude will be influenced by changes in the wind shear and the decrease in mean density with height. All else being equal, waves generated at lower levels will be more energetic due to the greater change in air density between the level of generation and the level at which they are observed. The momentum flux transported by convectively generated waves depends therefore on the mean atmospheric density at the level at which the waves are generated; if the velocity perturbations are identical in two different wave-generation regions, those waves generated lower in the atmosphere will transport more momentum.

In these simulations it appears that the waves emanate from a region just below the top of the storm near the elevation of the level of neutral buoyancy, which seems to constitute the top of the wave generation region. In the TOGA COARE simulations the level of neutral buoyancy is near $z = 12$ km, in the Hector simulations it is near $z = 15$ km, and in the COPT-81 simulations it is near 16 km. The decrease in mean atmospheric density between 12 and 16 km implies that waves originating at these two levels with the same initial amplitude, will have amplitudes that differ by approximately a factor of $(2)^{1/2}$ at any height above 16 km. The TOGA COARE updrafts are roughly a factor of $(2)^{-1/2}$ weaker than those in the COPT-81 simulation, so at least in these simulations, the differences in the strength of the storms are almost exactly compensated by the differences in the depths of the storms, and the wave amplitude at a given level several kilometers above each of these storms is nearly identical. On average, less energetic tropical convective complexes tend to have lower levels of neutral buoyancy, so this type of compensation is likely to moderate the case-to-case variations in the strength of convectively generated gravity waves throughout the Tropics—a fortuitous circumstance that might facilitate the parameterization of such waves in larger-scale models.

Using the statistical climatology of tropical mesoscale convective systems, compiled by Mohr and Zipser (1996), PDAH estimated that convectively triggered gravity waves could account for roughly 30% of the forcing required for the downward propagation of the eastward phase of the QBO and roughly 15% of the forcing for the westward phase. They also suggested that these estimates should be considered as upper limits since, although their simulated storm was weaker than typical Hector events, it was still stronger than the average tropical MCS. Reapplying the PDAH methodology using the additional storm types considered in this study, we estimate that if the typical tropical MCS had the characteristics of the simulated TOGA COARE storm, convectively triggered gravity waves could account for approximately 15% of the forcing required for the downward propagation of the eastward phase QBO and for about 25% of the forcing for the westward phase. The figures for the COPT-81 case are roughly 40% for the eastward phase and 25% for the westward phase.

Nevertheless, as evident in this study, the strength of a MCS is not the only important factor determining its potential to generate gravity waves capable of influencing the QBO. Indeed, variations in storm intensity may be less significant than initially supposed because, as just discussed, high-CAPE storms may also be deep storms that trigger gravity waves at elevations where the mean atmospheric density is comparatively low. The structure of the tropospheric zonal wind profile also plays an important role in determining the fraction of the momentum carried by the gravity waves that will be deposited within the QBO shear layers. This is clearly the case in the TOGA COARE simulations where, due to the eastward propagation of the storm, a large portion of the eastward momentum flux is carried by waves with phase speeds that exceed the maximum winds in the eastward QBO phase (Fig. 23a). Due to these complexities, it is not possible to present a more precise numerical estimate of the influence of convectively generated gravity waves on the QBO than that already given in PDAH.

8. Summary and conclusions

The strength and distribution of stratospheric gravity waves generated by tropical convective systems has been examined through 3D numerical simulations. Two prototypical convective events were considered: a squall line over the western Pacific warm pool observed during TOGA COARE and a West African squall line studied during the COPT-81 project. The gravity waves triggered by these squall lines were also compared with those generated by an idealized Hector storm similar to that previously investigated in PDAH. The wind shear in the stratosphere overlying each of these convective events was systematically varied to include a profile typical of either the westward phase of the QBO, the eastward phase of the QBO, or a control case in which there was no wind shear in the stratosphere and all waves were free to propagate vertically without undergoing critical level absorption.

The COPT-81 and Hector storms developed in continental or continentally modified environments with large values of CAPE, and our simulations of these storms exhibited maximum updraft velocities on the order of 20–25 m s^{-1}. The TOGA COARE storm occurred in a marine environment with more modest CAPE, and the maximum updrafts in the TOGA COARE simulations were correspondingly weaker (15–20 m s^{-1}). Somewhat surprisingly, all three types of convective events generated stratospheric gravity waves with similar amplitudes (in the control-case simulations). The more intense convection in the COPT-81 and Hector events extended to greater heights and as a consequence, the stratospheric gravity waves generated by these storms originated in a region of lower atmospheric density than the waves triggered by the weaker TOGA COARE convection. In these particular simulations, the tendency for stronger storms to generate larger amplitude gravity waves was offset by the tendency of the stronger storms to extend to greater heights. It is not clear whether a similar compensation between updraft strength and storm depth might be expected in a larger sample of tropical convective events. Indeed the data analyzed by Vincent and Alexander (2000) do not show evidence of such compensation, but rather suggest that, at least over the Maritime continent, there is a positive correlation between stronger stratospheric gravity-wave activity and deeper storms with colder cloud tops.

A series of additional experiments were also conducted to examine the azimuthal distribution of the stratospheric gravity waves launched by the TOGA COARE storm in an environment with no stratospheric wind shear but different storm-relative stratospheric winds. These simulations suggest that, although other factors may be nonnegligible, the single most important factor determining the azimuthal distribution of gravity waves launched by the storm is the storm-relative stratospheric wind. Strong storm-relative winds not only skewed the distribution of simulated gravity waves, they also led to the generation of storm-relative stationary waves, akin to mountain waves, possibly through an obstacle effect. However, we must stress that the obstacle effect accounts for only a small portion of the momentum flux, even in the presence of strong storm-relative winds.

When the stratospheric wind profile contained shear layers characteristic of the eastward or westward phase of the QBO, convectively generated waves propagating in the direction of the shear vector at speeds less than the upper-level flow experienced critical-level absorption within the shear layer. Nevertheless, in those simulations with open lateral boundaries the vertical momentum-flux divergence associated with critical-level absorption was not even roughly balanced by the mean-flow deceleration. As in the earlier simulations reported by PDAH, the two largest terms in the domain-averaged momentum budget were the mean-flow deceleration and the difference in the dynamic pressure across the domain. In order to capture the change in the domain-averaged mean flow that must occur in response to vertical momentum-flux divergence in a closed system such as the earth's atmosphere, we also conducted simulations in periodic domains. The domain-averaged vertical momentum-flux profiles were very similar between the periodic and open-domain simulations, but as would be expected, in the periodic-domain simulations the vertical momentum-flux divergence almost exactly balanced the mean-flow deceleration.

The magnitude of the stratospheric mean-flow deceleration associated with the critical-level absorption of convectively generated gravity waves varied somewhat between the TOGA COARE, the COPT-81, and the Hector events, depending on both the structure of the tropospheric zonal wind profile and the strength of the convective cells. Given the case-to-case variation evident in these simulations and the uncertainties in the available climatologies of tropical convective systems, it is not possible to rigorously improve the precision of the estimate presented in PDAH for the impact of convectively induced gravity-wave drag on the QBO. To be specific, the results from the additional simulations presented in this paper are consistent with the PDAH's tentative estimate that convectively induced gravity waves could account for roughly 30% of the forcing required for the downward propagation of the eastward phase of the QBO and roughly 15% of the forcing for the westward phase.

Acknowledgments. The authors acknowledge fruitful discussions with Joan Alexander and Jim Holton and thank Yadwiga Beres for making her results available to us prior to publication. This research was supported by the National Science Foundation NSF Grant ATM-9979241.

APPENDIX A

Temperature, Moisture, and Wind Profiles for the TOGA COARE Control Case

z (m)	θ (K)	q_v (gr/kg)	u (m s^{-1})	v (m s^{-1})
50	302.9	23.3	0.1	−6.5
154	302.9	22.8	1.2	−6.5
267	303.0	22.1	2.4	−6.5
389	303.0	21.0	3.6	−6.5
522	303.1	20.1	5.0	−6.5
665	303.2	19.2	6.5	−6.5
821	303.4	18.0	7.9	−6.4
990	303.6	16.4	8.9	−6.0
1172	303.9	14.7	10.1	−5.7
1370	304.4	13.5	10.9	−5.2
1585	305.0	12.7	11.5	−4.7
1817	305.9	12.1	12.0	−4.2
2069	307.1	11.5	12.1	−3.8
2342	308.4	10.9	11.9	−3.4
2638	310.1	10.2	11.3	−3.1
2958	311.9	9.5	10.7	−2.8
3305	313.9	8.8	10.0	−2.6
3681	316.2	8.1	9.4	−2.4
4089	318.4	7.3	8.8	−2.3
4530	320.6	6.6	8.0	−2.1
5009	323.1	5.8	7.2	−1.8
5527	325.8	5.0	6.4	−1.5
6089	328.7	4.3	5.6	−1.2
6697	331.8	3.5	4.9	−0.8
7357	335.2	2.7	4.1	−0.4
8050	338.3	1.9	3.3	−0.0
8750	341.2	1.3	2.6	0.6
9450	343.9	0.9	1.8	1.1
10 150	346.0	0.5	1.1	1.6
10 850	347.5	0.3	0.5	2.0
11 550	348.7	0.1	−0.4	2.3
12 250	350.1	0.0	−1.1	2.6
12 950	351.4	0.0	−1.7	3.1
13 650	352.4	0.0	−2.5	3.5
14 350	353.0	0.0	−3.6	4.2
15 050	355.6	0.0	−4.6	3.9
15 750	358.6	0.0	−4.9	3.5
16 450	364.2	0.0	−4.9	0.8
17 150	377.6	0.0	−4.9	0.0
18 550	407.4	0.0	−4.9	0.0
19 950	439.5	0.0	−4.9	0.0
21 350	454.1	0.0	−4.9	0.0
22 750	511.5	0.0	−4.9	0.0
25 550	595.2	0.0	−4.9	0.0
28 350	692.7	0.0	−4.9	0.0
31 150	806.1	0.0	−4.9	0.0
33 950	938.1	0.0	−4.9	0.0
36 750	1091.6	0.0	−4.9	0.0
39 550	1270.4	0.0	−4.9	0.0
42 350	1478.4	0.0	−4.9	0.0

p_0 = 1004 mb.

APPENDIX B

Temperature, Moisture, and Wind Profiles for the COPT-81 Control Case

z (m)	θ (K)	q_v (gr/kg)	u (m s^{-1})	v (m s^{-1})
50	303.1	16.5	−0.1	2.5
154	303.2	15.8	−0.4	2.4
267	303.2	15.7	−1.1	2.2
389	303.3	15.4	−1.9	1.9
522	303.5	15.4	−2.7	1.6
665	303.7	15.4	−3.6	1.4
821	304.0	14.5	−4.6	1.0
990	304.4	13.9	−5.6	0.7
1172	304.9	13.0	−6.7	0.3
1370	305.5	11.9	−8.0	−0.5
1585	306.5	10.7	−9.3	−0.9
1817	307.5	9.7	−10.7	−1.4
2069	308.7	8.8	−11.8	−1.9
2342	309.8	7.9	−11.3	−2.4
2638	311.0	7.0	−10.7	−2.9
2958	312.3	6.1	−10.2	−3.5
3305	313.7	5.2	−9.55	−4.1
3681	315.2	4.4	−8.87	−4.6
4089	316.9	3.5	−8.28	−4.2
4530	319.0	2.4	−8.22	−3.7
5009	321.5	1.4	−8.14	−2.6
5527	324.1	0.9	−8.07	−2.3
6089	327.4	1.2	−8.12	−2.0
6697	331.0	1.4	−9.0	−1.7
7357	334.0	1.2	−10.0	−1.7
8050	336.9	0.7	−10.1	−1.8
8750	339.3	0.3	−11.2	−1.7
9450	341.8	0.1	−11.4	−1.2
10 150	343.6	0.0	−12.0	−0.6
10 850	345.8	0.0	−13.3	−0.3
11 550	348.0	0.0	−14.5	−0.2
12 250	349.8	0.0	−15.0	−0.2
12 950	350.7	0.0	−14.0	−0.1
13 650	351.7	0.0	−13.0	−0.07
14 350	353.2	0.0	−12.0	−0.1
15 050	357.5	0.0	−11.0	−0.0
15 750	370.2	0.0	−10.0	−0.0
16 450	383.1	0.0	−10.0	0.0
17 150	396.8	0.0	−10.0	0.0
18 550	425.6	0.0	−10.0	0.0
19 950	456.6	0.0	−10.0	0.0
21 350	489.8	0.0	−10.0	0.0
22 750	525.4	0.0	−10.0	0.0
25 550	604.5	0.0	−10.0	0.0
28 350	687.8	0.0	−10.0	0.0
31 150	801.1	0.0	−10.0	0.0
33 950	933.1	0.0	−10.0	0.0
36 750	1086.6	0.0	−10.0	0.0
39 550	1265.4	0.0	−10.0	0.0
42 350	1473.4	0.0	−10.0	0.0

p_0 = 960 mb.

REFERENCES

Alexander, M. J., and L. Pfister, 1995: Gravity wave momentum flux in the lower stratosphere over convection. *Geophys. Res. Lett.*, **22,** 2029–2032.

——, and J. R. Holton, 1997: A model study of zonal forcing in the equatorial stratosphere by convectively induced gravity waves. *J. Atmos. Sci.*, **54,** 408–419.

——, J. H. Beres, and L. Pfister, 2000: Tropical stratospheric gravity wave activity and relationships to clouds. *J. Geophys. Res.*, **105,** 22 299–22 309.

Baldwin, M. P., and Coauthors, 2001: The quasi-biennial oscillation. *Rev. Geophys.*, **39,** 179–229.

Clark, T. L., T. Hauf, and J. P. Kuettner, 1986: Convectively forced internal gravity waves: Results from two-dimensional numerical experiments. *Quart. J. Roy. Meteor. Soc.*, **112,** 899–925.

Dunkerton, T. J., 1997: The role of gravity waves in the quasi-biennial oscillation. *J. Geophys. Res.*, **102,** 26 053–26 076.

Durran, D. R., 1999: *Numerical Methods for Wave Equations in Geophysical Fluid Dynamics.* Springer Verlag, 465 pp.

Fovell, R., D. R. Durran, and J. R. Holton, 1992: Numerical simulations of convectively generated gravity waves. *J. Atmos. Sci.,* **49,** 1427–1442.

Gill, A. E., 1982: *Atmosphere–Ocean Dynamics.* Academic Press, 662 pp.

Lane, T. P., M. J. Reeder, and T. L. Clark, 2001: Numerical modeling of gravity wave generation by deep tropical convection. *J. Atmos. Sci.,* **58,** 1249–1274.

Mason, P. J., and R. I. Sykes, 1982: A two-dimensional numerical study of horizontal roll vortices in an inversion capped planetary boundary layer. *Quart. J. Roy. Meteor. Soc.,* **108,** 801–823.

Mohr, K. I., and E. J. Zipser, 1996: Mesoscale convective systems defined by their 85-Ghz ice scattering signature: Size and intensity comparison over tropical oceans and continents. *Mon. Wea. Rev.,* **124,** 2417–2437.

Piani, C., D. R. Durran, M. J. Alexander, and J. R. Holton, 2000: A numerical study of three-dimensional gravity waves triggered by deep tropical convection and their role in the dynamics of the QBO. *J. Atmos. Sci.,* **57,** 3689–3702.

Redelsperger, J.-L., and J.-P. Lafore, 1988: A three-dimensional simulation of a tropical squall line: Convective organization and thermodynamic vertical transport. *J. Atmos. Sci.,* **45,** 1334–1356.

Roux, F., 1988: The West African squall line observed on 23 June 1981 during COPT-81: Kinematics and thermodynamics of the convective region. *J. Atmos. Sci.,* **45,** 406–426.

Trier, S. B., W. C. Skamarock, M. A. LeMone, D. B. Parsons, and D. P. Jorgensen, 1996: Structure and evolution of the 22 February 1993 togacoare squall line: Numerical simulations. *J. Atmos. Sci.,* **53,** 2861–2886.

Vincent, R. A., and M. J. Alexander, 2000: Gravity waves in the tropical lower stratosphere: An observational study of seasonal and interannual variability. *J. Geophys. Res.,* **105,** 17 971–17 982.